

See discussions, stats, and author profiles for this publication at: <https://www.researchgate.net/publication/49807799>

# Polymorphism in Self-Assembled AB(6) Binary Nanocrystal Superlattices

ARTICLE *in* JOURNAL OF THE AMERICAN CHEMICAL SOCIETY · FEBRUARY 2011

Impact Factor: 12.11 · DOI: 10.1021/ja108708v · Source: PubMed

---

CITATIONS

40

READS

98

## 3 AUTHORS, INCLUDING:



Xingchen Ye

University of California, Berkeley

57 PUBLICATIONS 2,726 CITATIONS

[SEE PROFILE](#)



Christopher B Murray

University of Pennsylvania

259 PUBLICATIONS 26,931 CITATIONS

[SEE PROFILE](#)

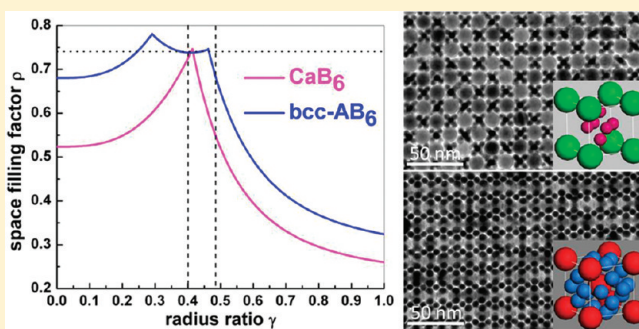
# Polymorphism in Self-Assembled $\text{AB}_6$ Binary Nanocrystal Superlattices

Xingchen Ye,<sup>†,‡</sup> Jun Chen,<sup>§,‡</sup> and Christopher B. Murray<sup>\*,†,§</sup>

<sup>†</sup>Department of Chemistry and <sup>§</sup>Department of Materials Science and Engineering, University of Pennsylvania, Philadelphia, Pennsylvania 19104, United States

Supporting Information

**ABSTRACT:** We report the formation and systematic structural characterization of a new  $\text{AB}_6$  polymorph with the body-centered cubic (bcc) symmetry in binary nanocrystal superlattices (BNSLs). The bcc- $\text{AB}_6$  phase, lacking any atomic analogue, is isomeric to certain alkali-metal intercalation compounds of fullerene  $\text{C}_{60}$  (e.g.,  $\text{K}_6\text{C}_{60}$ ). On the basis of the space-filling principle, we further tailor the relative phase stability of the two  $\text{AB}_6$  polymorphs— $\text{CaB}_6$  and bcc- $\text{AB}_6$ —from coexistence to phase-pure bcc- $\text{AB}_6$ , highlighting the entropic effect as the main driving-force of the self-organization of BNSLs. We also discuss the implication of surface topology studies and the observation of twinning and preferential orientation in bcc- $\text{AB}_6$  on the growth mechanism of BNSLs. Furthermore, the connection between the bcc- $\text{AB}_6$  phase and the (3<sup>2</sup>.4.3.4) Archimedean tiling shows the promise of further exploration on the structural diversity (both periodic and aperiodic) in this emerging class of metamaterials. The identification and the ability to tune the relative phase stability of polymorphic structures provide a unique opportunity to engineer the interparticle coupling through controlled clustering and/or interconnectivity of sublattice in BNSLs with identical stoichiometry.



## 1. INTRODUCTION

Controlled synthesis and organization of molecules, supramolecular complexes, and inorganic nanomaterials into functional superstructures or architectures have been the focus of many materials research efforts.<sup>1–8</sup> Ordered arrays of colloidal nanocrystals (NCs) not only provide opportunities to study self-assembly processes but also offer a low-cost bottom-up approach for integration of nanoscale building blocks into functional devices, including field-effect transistors,<sup>9</sup> thermoelectric converters,<sup>10</sup> light-emitting diodes,<sup>11,12</sup> photodetectors,<sup>13</sup> solar cells,<sup>14</sup> plasmonic waveguides<sup>15</sup> and sensors,<sup>16,17</sup> magnetic recording media.<sup>18</sup> In particular, the modular assembly of two different NCs into binary nanocrystal superlattices (BNSLs) has recently attracted fast-growing research interests, as it provides a versatile means to capture the beauty as well as structural diversity at the nanoscale and more importantly, to access a diverse array of metamaterials with programmable physical properties.<sup>19–24</sup>

From a different perspective, NCs can often be regarded as “artificial atoms” and NC superlattices can serve as a convenient platform to help understand a variety of phenomena and dynamic processes during crystal formation in atomic solids that are usually very hard to visualize in real space.<sup>25</sup> Polymorphism, the ability of a material to exist in more than one form in the solid state, has profound implications for advances of materials science and technology. Perhaps the most amazing demonstration is the

polymorphism of carbon. Graphite and diamond are traditional polymorphs, but the discoveries of others such as  $\text{C}_{60}$ ,<sup>26</sup> carbon nanotubes,<sup>27</sup> and the most recent one—graphene<sup>28</sup>—have stimulated enormous research activities on the chemistry, physics, and technological applications of these materials and their derivatives. It is notable that alkali-metal fullerenes using  $\text{C}_{60}$  building blocks show dramatic structure–property differences depending on the polymorph: face-centered-cubic  $\text{K}_3\text{C}_{60}$  is superconducting,<sup>29</sup> while no superconductivity is observed in body-centered cubic (bcc)  $\text{K}_3\text{C}_{60}$ .<sup>30</sup>

In this work, we report an experimental study of polymorphism in  $\text{AB}_6$  BNSLs self-assembled from monodisperse Au and  $\text{Fe}_3\text{O}_4$  NCs. We identify a new  $\text{AB}_6$  polymorph exhibiting bcc lattice symmetry, which complements the known simple cubic  $\text{CaB}_6$  phase. The size ratio between small and large NCs is employed to adjust the relative phase stability between the two  $\text{AB}_6$  polymorphs, resulting in the reproducible formation of phase-pure bcc- $\text{AB}_6$  BNSLs.

## 2. EXPERIMENTAL SECTION

### 2.1. Synthesis and Characterization of Nanocrystals.

All syntheses were performed using standard Schlenk techniques. The

Received: October 6, 2010

Published: February 3, 2011

$\text{Fe}_3\text{O}_4$  NCs were synthesized using the method developed by Hyeon et al.<sup>31</sup> The Au NCs were synthesized on the basis of the method developed by Yin et al.<sup>32</sup> for Ag NCs and a digestive ripening route developed by Klabunde et al.<sup>33</sup> for Au NCs. Briefly, 0.08 g of  $\text{AuCl}_3$  (99.99%, Aldrich) was dissolved in a mixture of 3 mL of oleylamine (70%, Aldrich) and 6 mL of *o*-dichlorobenzene (99%, Acros Organics). The solution was then injected into a boiling mixture ( $\sim 181^\circ\text{C}$ ) of 0.4 g of 1,2-hexadecanediol (90%, Aldrich) and 12 mL of *o*-dichlorobenzene under nitrogen flow and vigorous magnetic stirring. The reaction mixture was subsequently maintained at  $165^\circ\text{C}$  for 90 s (for 4.6 nm Au NCs, relative standard deviation RSD < 6%) or 3 min (for 5.8 nm Au NCs, RSD < 5%) before it was cooled to room temperature using a water bath. After being isolated by adding ethanol and centrifugation, the Au NCs were then redispersed in 20 mL of toluene in the presence of 2 mL of 1-dodecanethiol (98%, Aldrich), and the mixture was refluxed for 15 min under nitrogen flow. Precipitation with ethanol allows the removal of excess 1-dodecanethiol and isolation of NCs. Finally, the  $\text{Fe}_3\text{O}_4$  and Au NCs were dissolved in trichloroethylene (TCE, Aldrich, 99.5%) with a NC concentration of  $\sim 1.5$  and  $\sim 0.5$  mg/mL, respectively. Particle number concentrations of NC solutions were estimated from thermal gravimetric analysis (TGA). Electrophoretic mobility measurements were performed on a Delsa Nano C system (Beckman Coulter).

**2.2. Preparation of Binary Nanocrystal Superlattices.** A TEM grid (300 mesh, Electron Microscopy Sciences) was placed at the bottom of a glass vial containing 10  $\mu\text{L}$  of TCE solution of  $\text{Fe}_3\text{O}_4$  NCs, 15–30  $\mu\text{L}$  of TCE solution of Au NCs, and 100  $\mu\text{L}$  of TCE. The tilted vial ( $\sim 45^\circ$  tilt angle) was left inside a vacuum oven under reduced pressure ( $\sim 30$  kPa) at  $50^\circ\text{C}$ . The grid was taken out after 12 h for further structural analysis.

**2.3. Structural Characterization of Binary Nanocrystal Superlattices.** Transmission electron microscopy (TEM) images and electron diffraction patterns were taken on a JEM1400 transmission electron microscope operating at 120 kV. Tilting of the BNSL structures was performed using a model 2040 dual-axis TEM tomography holder (Fischione Instruments). Three-dimensional crystal structure models were built using Materials Studio 4.4 (Accelrys Software) and were compared with TEM images. Different projections were obtained by direct tilting of the built crystal structures. Electron diffraction simulation was performed using EMS software (Pierre Stadelmann). Scanning electron microscopy (SEM) was carried out on a JEOL 7500F high-resolution SEM. We also performed the two-dimensional Fourier transformation of the real-space TEM images to ensure consistency with the experimental small-angle electron diffraction patterns.

### 3. RESULTS AND DISCUSSION

**3.1. Self-Assembly and Systematic Structural Characterization of  $\text{CaB}_6$  and bcc- $\text{AB}_6$  BNSLs.** The three-dimensional (3D) structural models of  $\text{CaB}_6$  and bcc- $\text{AB}_6$  are shown in parts a and c of Figure 1, respectively. The  $\text{CaB}_6$  unit cell consists of a simple cubic lattice of large spheres with an octahedral cluster composed of six small spheres inside. On the other hand, the bcc- $\text{AB}_6$  unit cell consists of a body-centered cubic lattice formed by the large spheres, with the four small spheres forming a square on each of the six faces of the cube. Each large sphere is thus surrounded by 24 small spheres, and all small spheres are equivalent, sitting in the interstitial sites of distorted tetrahedral symmetry created by four large spheres. Therefore, the two  $\text{AB}_6$  polymorphs differ in the arrangement of both large and small spheres as well as the lattice symmetry. The bcc- $\text{AB}_6$  structure was first discovered in certain alkali-metal intercalation compounds of fullerene  $\text{C}_{60}$  (e.g.,  $\text{K}_6\text{C}_{60}$ ,  $\text{Cs}_6\text{C}_{60}$  etc.).<sup>30</sup> Later on, it

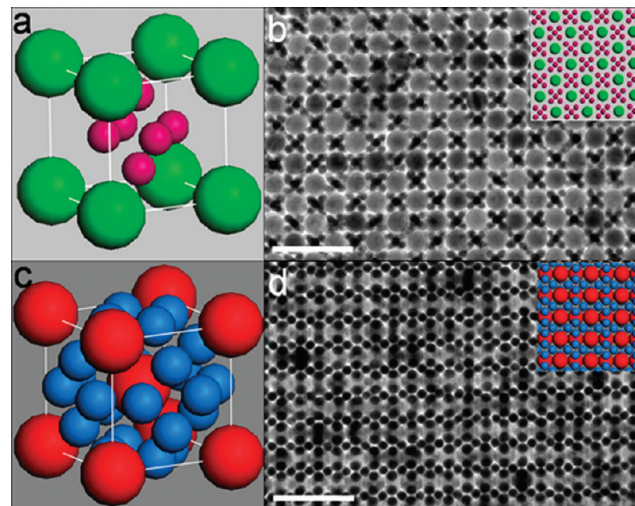


**Figure 1.** Structural models and TEM images of  $\text{AB}_6$  BNSLs self-assembled from 4.6 nm Au and 14.0 nm  $\text{Fe}_3\text{O}_4$  NCs. Unit cells of (a)  $\text{CaB}_6$  and (c) bcc- $\text{AB}_6$  structures. (b) TEM image and structural model (inset) of the [001] projection of  $\text{CaB}_6$  BNSLs. (d) TEM image and structural model (inset) of the [110] projection of bcc- $\text{AB}_6$  BNSLs. The scale bars represent 50 nm.

was observed as a stable phase of binary mixtures of hard spheres at size ratio  $\sim 0.40$ <sup>34</sup> and also theoretically predicted and identified in colloidal crystals composed of micrometer-sized oppositely charged particles.<sup>35</sup> Parts b and d of Figure 1 show the TEM images of the commonly observed projections of BNSLs isostructural with  $\text{CaB}_6$  and bcc- $\text{AB}_6$  phases, respectively. Both structures are self-assembled from 4.6 nm Au and 14.0 nm  $\text{Fe}_3\text{O}_4$  NCs (RSD < 4%) under slow evaporation of a combined TCE solution (see section 2.2). Importantly, they coexist in a single sample under certain preparation conditions (e.g., when solutions with  $\sim 1:8$   $\text{Fe}_3\text{O}_4$ -to-Au NC number ratio are used). The TEM image shown in Figure 1b matches the [001] projection of the  $\text{CaB}_6$  structure in which the  $(\text{Au})_6$  octahedral clusters are separated by the simple cubic packed  $\text{Fe}_3\text{O}_4$  NCs. Moreover, the characteristic alternating chains of Au and  $\text{Fe}_3\text{O}_4$  NCs shown in Figure 1d are consistent with the [110] projection of the bcc- $\text{AB}_6$  structure. This suggests a previously unidentified bcc polymorph of  $\text{AB}_6$  BNSL.

It has been shown that, in BNSLs, domains corresponding to either different crystal structures or different projections of the same crystal structures can be observed in a single sample.<sup>24,36–44</sup> The visual comparison of TEM images with the projections of modeled crystal structures could lead to misinterpretation of the 3D arrangement of NCs in BNSLs. Therefore, to unambiguously assign the structure of BNSLs, we need to obtain local and global structural information from BNSL domains.<sup>41,42,45</sup> Here we apply the general structural characterization framework to the study of polymorphism in  $\text{AB}_6$  BNSLs.<sup>41</sup> The “toolset” includes a combination of techniques: stereographic projection is used as a crystallographic tool to design series tilt path. TEM images and small-angle electron diffraction (SAED) patterns acquired during series tilting provide direct real-space and reciprocal-space information of the BNSL structures. Modeling of crystallographic projections and simulation of electron diffraction patterns help interpret and confirm the experimental data. In this study, we also use SEM to investigate the surface topology of the bcc- $\text{AB}_6$  BNSLs, which provides complementary and particularly

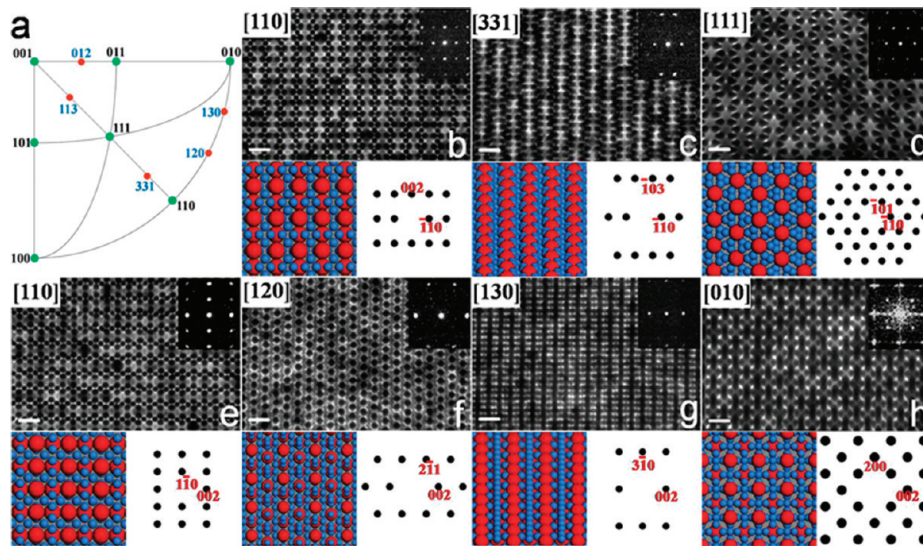


**Figure 2.** Series tilting of bcc-AB<sub>6</sub> BNSLs self-assembled from 4.6 nm Au and 14.0 nm Fe<sub>3</sub>O<sub>4</sub> NCs. (a) Stereographic projection of the cubic crystal system. The projection plane is normal to the [001] direction. Tilt series 1 (b–d) starts from the [110] zone axis and tilts around the [110] direction. Tilting sequence: [110]→[331]→[111]. After 90° in-plane rotation of b, tilt series 2 (e–h) starts from the [110] zone axis and tilts around the [001] direction. Tilting sequence: [110]→[120]→[130]→[010]. Below each TEM image (inset of each is the corresponding small-angle ED pattern) are the corresponding structural model (left) and simulated ED pattern (right) except that the upper-right inset of part h is the corresponding fast Fourier transform pattern. All scale bars represent 20 nm.

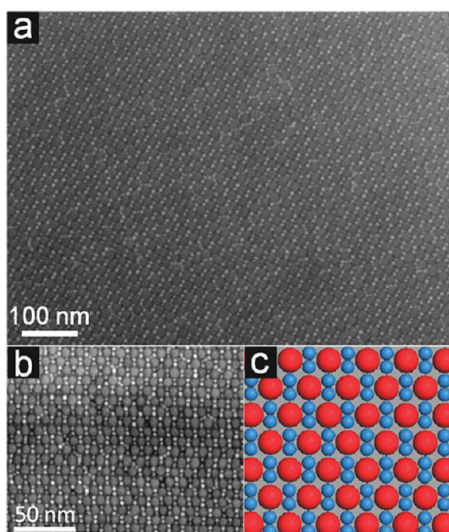


**Figure 3.** (a, b) SEM images of the bcc-AB<sub>6</sub> BNSLs self-assembled from 4.6 nm Au and 14.0 nm Fe<sub>3</sub>O<sub>4</sub> NCs. (c) Structural model of the (110) plane of CaB<sub>6</sub> BNSLs.

useful structural information for the identification of the bcc-AB<sub>6</sub> polymorph.<sup>40</sup>

According to the stereographic projection of the cubic lattice (Figure 2a), we design two series tilting paths connecting low-index projections such as [001], [011], and [111] for the bcc-AB<sub>6</sub> BNSLs. The TEM images and SAED patterns of projections obtained during series tiltings are presented in Figure 2. The correspondence between the TEM images of six different crystallographic projections and the models and the consistency between real and simulated SAED patterns confirm the bcc-AB<sub>6</sub> structure. Furthermore, the SEM images acquired from bcc-AB<sub>6</sub> BNSLs (Figures 3a,b and S4, Supporting Information) display a particle packing motif different from what is observed in the TEM

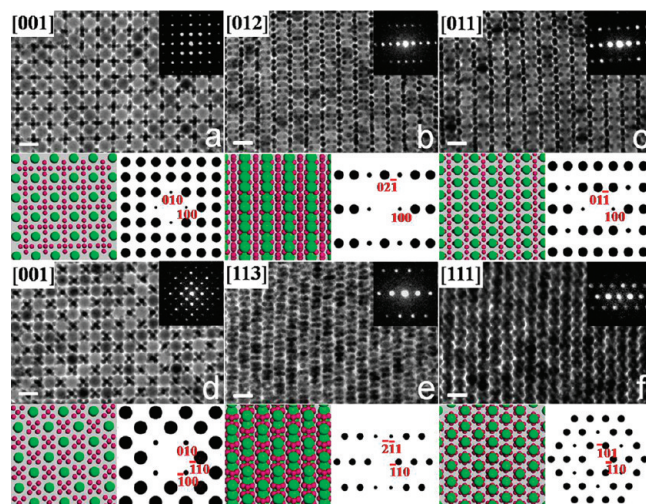


**Figure 4.** Series tilting of CaB<sub>6</sub> BNSLs self-assembled from 4.6 nm Au and 14.0 nm Fe<sub>3</sub>O<sub>4</sub> NCs. Tilt series 1 (a–c) starts from the [001] zone axis and tilts around the [100] direction. Tilting sequence: [001]→[012]→[011]. After 45° in-plane rotation of a, tilt series 2 (d–f) starts from the [001] zone axis and tilts around the [110] direction. Tilting sequence: [001]→[113]→[111]. Below each TEM image (inset of each is the corresponding small-angle ED pattern) are the corresponding structural model (left) and simulated ED pattern (right). All scale bars represent 20 nm.

images. The arrangement of surface NCs matches the model of the (110) plane (Figure 3c). These electron microscopy surveys yield a unique structural assignment of the BNSLs shown in Figure 1d as bcc-AB<sub>6</sub>.

To further compare the structural difference among various projections of the two AB<sub>6</sub> polymorphs, we perform series tilting experiments on CaB<sub>6</sub> BNSLs (Figure 4). Although formation of the CaB<sub>6</sub> structure has been reported in PbSe–Pd and

$\text{Fe}_2\text{O}_3$ –Au BNSLs,<sup>22,23</sup> to the best of our knowledge, no TEM tilting study has been carried out. As shown in Figure 4, TEM images of other projections of  $\text{CaB}_6$  BNSLs including [012], [011], [113], and [111] projections are seen after series tilting from the [001] projection. Again all the projections are in accordance with the structural models, further confirming the 3D packing of NCs in the  $\text{CaB}_6$  structure.

**3.2. Tuning of Polymorphism in  $\text{AB}_6$  BNSLs Based upon Packing Density Consideration.** To date, various interparticle interactions have been taken into account to understand the formation mechanism and structural diversity of BNSLs, including free volume entropy (space-filling principle),<sup>38,39,41,42,44,46</sup> electrostatic coulomb interactions,<sup>21,22,38,47</sup> dipole–dipole interactions,<sup>38,46</sup> van der Waals forces between the NCs<sup>38,42</sup> and hydrophobic interactions between the ligands.<sup>38,39</sup> Among these, the free volume entropy and the electrostatic interactions have been shown to be able to contribute significantly to the overall energy landscape during self-assembly of NCs and thus affect the structure of BNSLs.<sup>21,22,46</sup> To explore the contribution of electrostatic interaction to the relative phase stability of the two  $\text{AB}_6$  polymorphs, we performed electrophoretic mobility measurements on Au and  $\text{Fe}_3\text{O}_4$  NCs dispersed in TCE solvent. The  $\text{Fe}_3\text{O}_4$  and Au NCs employed in this study are capped with oleic acid and 1-dodecanethiol molecules, respectively. The results, as shown in Figure S5 (Supporting Information), demonstrate that both NCs are nearly electrostatically neutral. Therefore, we believe that the formation of both  $\text{CaB}_6$  and bcc- $\text{AB}_6$  BNSLs in this study is mainly entropy-driven (see discussion below).

The total entropy of a hard sphere system consists of two parts: the configurational entropy and the free volume entropy.<sup>48,49</sup> The former relates to the degree of spatial ordering and the latter is associated with the free space available for individual particle's local movements. Entropy-driven crystallization is achieved when the increase in free volume entropy is greater than the decrease in configurational entropy. This simple entropic origin is the driving force for superlattice formation in hard sphere systems.<sup>48,50</sup> Superlattice structures with a higher packing density should have a larger free volume per particle, thus offering a larger contribution to the entropy and hence a lower free energy. Therefore, the ensemble of hard spheres should adopt an ordered lattice structure that maximizes the packing density.<sup>51–53</sup>

As far back as the 1960s, Parthé used the packing arguments to explain the phase stability of some binary intermetallic alloys.<sup>54</sup> Later on in the 1980s, Sanders and Murray reported observations of long-range ordered close-packed structures in natural opals composed of silica spheres of two different sizes.<sup>55,56</sup> These stimulated theoretical efforts where the packing density of the observed structures (namely  $\text{AlB}_2$  and  $\text{NaZn}_{13}$ ) was calculated in more detail.<sup>57</sup> Since most sterically stabilized (uncharged) colloidal particles can be approximated as hard spheres,<sup>58,59</sup> we extend the geometrical analysis of Murray and Sanders to the bcc- $\text{AB}_6$  phase. This provides a good estimate of the entropic contribution to the phase stability of the bcc- $\text{AB}_6$  structure. The space-filling curves for the bcc- $\text{AB}_6$  and  $\text{CaB}_6$  structures ( $\rho$  versus  $\gamma$ , where  $\rho$  = space-filling factor and  $\gamma$  = radius ratio between small and large spheres) are shown in Figure 5a.

In the case of the bcc- $\text{AB}_6$  structure, the first branch of the space filling curve corresponds to the low  $\gamma$  region where there are only A–A contacts. Here B spheres are small enough and

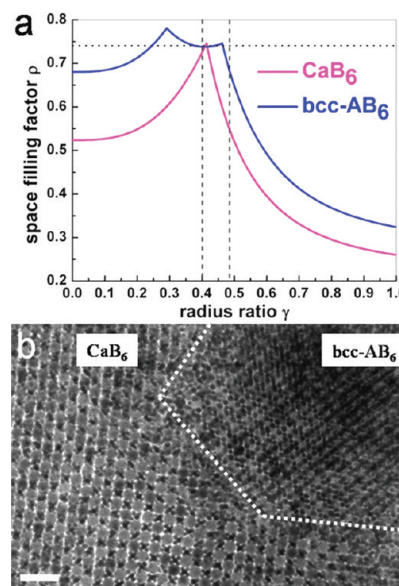


**Figure 5.** (a) Space-filling curves of  $\text{CaB}_6$  and bcc- $\text{AB}_6$  structures. The horizontal dashed line represents the packing density  $\rho = 0.7405$  of the single-component close-packed structures. The vertical dashed lines denote the radius ratio  $\gamma$  studied in this work. (b) TEM image showing the coexistence of  $\text{CaB}_6$  and bcc- $\text{AB}_6$  structures in BNSLs self-assembled from 4.6 nm Au and 14.0 nm  $\text{Fe}_3\text{O}_4$  NCs. The scale bar represents 50 nm.

the lattice parameter is determined only by the radius of A spheres. The packing density of this region is given by

$$\rho = \frac{\sqrt{3}\pi}{8} (1 + 6\gamma^3)$$

The formula is valid until contacts between small and large spheres occur at  $\gamma \approx 0.291$ . Then the second branch of the space-filling curve corresponds to a situation where both A–A and A–B contacts occur, and the lattice parameter is determined by the size ratio  $\gamma$ . The packing density of this region is given by

$$\rho = \frac{5\sqrt{5}\pi}{24} (1 + 6\gamma^3)(1 + \gamma)^3$$

The upper limit of the second branch is reached when B–B contacts occur at  $\gamma \approx 0.462$ . The third branch corresponds to the situation where there are only B–B contacts, and the lattice parameter is solely determined by the radius of B spheres. The packing density of this region is given by

$$\rho = \frac{\sqrt{2}\pi}{96} (6 + \gamma^{-3})$$

The space-filling curve of the bcc- $\text{AB}_6$  structure features a high packing density zone with  $\rho \geq 0.7405$  (the packing density of single-component close-packed structures) in the region of  $0.245 < \gamma < 0.465$ . In this study, the effective size of NCs  $d_{\text{eff}}$  can be estimated as  $d_{\text{eff}} = d_{\text{core}} + 2d_{\text{shell}}$ , where  $d_{\text{core}}$  is the diameter of the inorganic core measured from TEM images and  $d_{\text{shell}}$  is the effective thickness of the ligand shell.<sup>38</sup> Therefore,  $d_{\text{eff}}$  of the 4.6 nm Au NCs is estimated to be  $\sim 6.3$  nm and  $d_{\text{eff}}$  of the 14.0 nm  $\text{Fe}_3\text{O}_4$  NCs is  $\sim 15.7$  nm, giving rise to a size ratio  $\gamma$  of  $\sim 0.40$ , which falls into the “stable zone” of the bcc- $\text{AB}_6$  structure. The same size ratio gives a packing fraction of  $\sim 0.738$ .

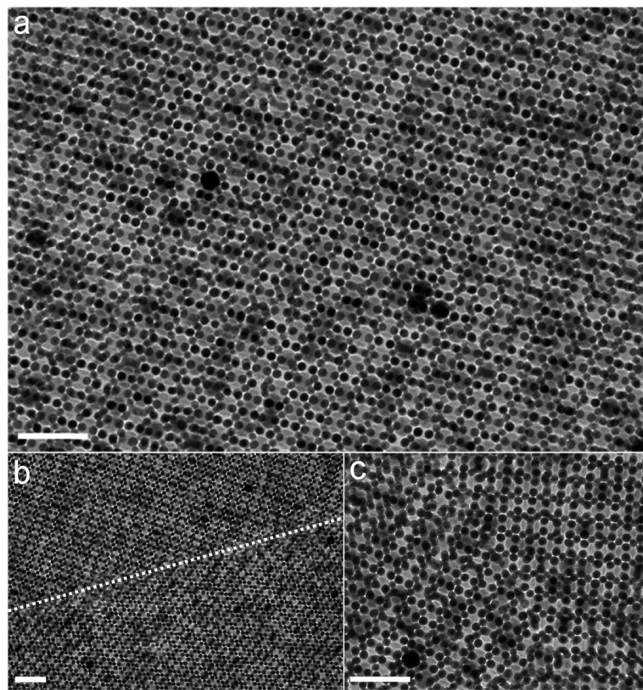


**Figure 6.** (a) TEM image of a [110]-oriented domain of bcc-AB<sub>6</sub> BNSLs self-assembled from 5.8 nm Au and 14.0 nm Fe<sub>3</sub>O<sub>4</sub> NCs. (b) Low and (c) high magnification TEM images of twin boundaries (highlighted with dash line) in bcc-AB<sub>6</sub> BNSLs self-assembled from 5.8 nm Au and 14.0 nm Fe<sub>3</sub>O<sub>4</sub> NCs. All scale bars represent 50 nm.

for the CaB<sub>6</sub> structure. Therefore, we believe that the reason for the polymorphism in AB<sub>6</sub> BNSLs is mainly due to the high packing density of both structures at this size ratio ( $\gamma \sim 0.40$ ), i.e., entropy-driven self-assembly process (Figures 5a,b and S6, Supporting Information). In addition, since the two polymorphs are different in their arrangement of both large and small NCs, the transformation between the two structures may involve a large change in free energy and/or a large activation barrier and thus is very unlikely. In fact, samples are found to retain the same structure after 2 years. This further supports that both polymorphs reported here are stable under ambient conditions.

Realizing the coexistence of two polymorphs in the same BNSL sample, we then target the possibility of tuning the relative phase stability between the two structures. The ability to make phase-pure BNSLs is essential to the development of rigorous structure–property relationships for this important class of metamaterials.<sup>24</sup> Size ratio<sup>46</sup> and temperature<sup>42,44</sup> have been invoked as structure-directing factors to affect the stability of one BNSL phase with respect to another. In this case, when the size of Au NCs is increased from 4.6 to 5.8 nm ( $d_{\text{eff}}$  from 6.3 to 7.5 nm) while the Fe<sub>3</sub>O<sub>4</sub> NCs are kept unchanged, long-range ordered bcc-AB<sub>6</sub> BNSLs are formed reproducibly without the coexistence of CaB<sub>6</sub> structure (Figures 6a and S7, Supporting Information). As predicted by the space-filling curves, the increase in the size of Au NCs (~20%) is effective enough to generate phase purity. The size ratio  $\gamma$  between the two components is shifted from  $\sim 0.40$  to  $\sim 0.48$ , leading to a significant difference between the packing densities of the two polymorphs (~25%).

**3.3. Preferential Orientation and Twinning in bcc-AB<sub>6</sub> BNSLs.** It has been shown that in BNSL samples, certain

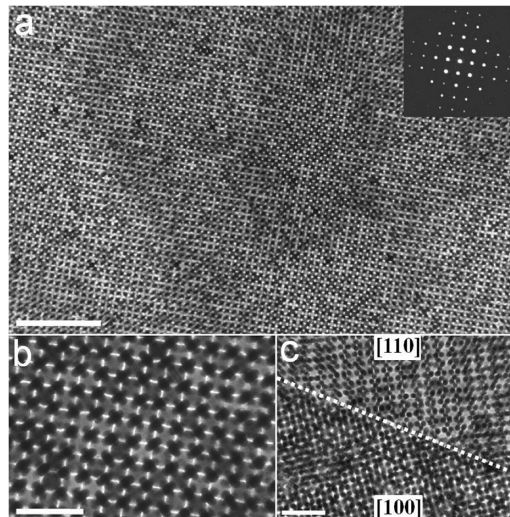


**Figure 7.** (a) Low and (b) high magnification TEM images of a [100]-oriented domain of bcc-AB<sub>6</sub> BNSLs self-assembled from 5.8 nm Au and 14.0 nm Fe<sub>3</sub>O<sub>4</sub> NCs. Inset of part a is the corresponding small-angle ED pattern. (c) TEM image showing the coexistence of [100]- and [110]-oriented domains in bcc-AB<sub>6</sub> BNSLs self-assembled from 5.8 nm Au and 14.0 nm Fe<sub>3</sub>O<sub>4</sub> NCs. Scale bars: (a) 200 nm, (b) 50 nm, and (c) 50 nm.

low-index crystallographic projections can be predominate over others, depending on the structure of the BNSL. For example, the [100]- and [110]-oriented domains are statistically more probable than others in ico-AB<sub>13</sub> BNSLs,<sup>41</sup> while [001] can be the dominant projection in AlB<sub>2</sub>-type BNSLs.<sup>40</sup> Chen et al. suggested that coexistence of different projections in BNSL samples might be a result of local fluctuations of NC number ratio and concentration during drying,<sup>46</sup> but a consensus on the dominant factors for preferential orientation has not been reached.

In the case of AB<sub>6</sub> BNSLs self-assembled from 4.6 nm Au and 14.0 nm Fe<sub>3</sub>O<sub>4</sub> NCs, we observe exclusively the [100]-oriented domains for CaB<sub>6</sub> BNSLs (Figure S8, Supporting Information) and the [110]-oriented domains for bcc-AB<sub>6</sub> BNSLs (Figure S9, Supporting Information). However, in bcc-AB<sub>6</sub> BNSLs self-assembled from 5.8 nm Au and 14.0 nm Fe<sub>3</sub>O<sub>4</sub> NCs, we also observe [100]-oriented domains (Figures 7 and S10, Supporting Information), yet they are much less probable compared to [110]-oriented domains (based upon statistical analysis of  $\sim 400$  domains from 15 samples). Series tilting experiments starting from [100]-oriented domains in untilted samples further confirm the bcc-AB<sub>6</sub> structure (Figure S11, Supporting Information). The preferential orientation in AB<sub>6</sub> BNSLs might be the result of the lowest energy crystallographic planes in the respective phases, yet we are reluctant to draw any conclusions before in-depth theoretical analysis and further experimental studies are carried out. On the other hand, these well-oriented BNSL facets provide a potential platform for the controlled growth of heterostructured BNSLs through colloidal epitaxy.<sup>60</sup>

More interestingly, as shown in Figures 6b,c and S7 (Supporting Information), it is commonly seen in the bcc-AB<sub>6</sub> BNSL samples that the lateral extension of the [110]-oriented domains is often disrupted by the mirror reflection of the planes across a sharp interface, i.e., twin boundary. This is in stark contrast with the typical mosaic texture with narrow and often amorphous boundaries separating different oriented domains in other types of BNSLs.<sup>38,41</sup> Rupich et al. recently reported the size-dependent multiple twinning in self-assembled single-component NC

superlattices, demonstrating the potential of using colloidal NCs as model systems for the study of not only periodic ordering but also phenomena such as faceting, defects, and twinning that are present in atomic crystals.<sup>61</sup> As manifested in Figure S12 (Supporting Information), the presence of terraces and twin planes between [110]-oriented domains of the bcc-AB<sub>6</sub> BNSL may imply that the BNSLs grow through a “quasi” layer-by-layer mode, where the addition of a new layer of NCs occurs after substantial lateral growth of the underlying layer.

**3.4. Connections of bcc-AB<sub>6</sub> Structure to (3<sup>2</sup>.4.3.4) Archimedean Tiling in BNSLs.** The recently discovered dodecagonal quasicrystal BNSLs not only are beautiful in their structural complexity but may provide more universal insights into the formation of a broad family of quasicrystalline and aperiodic structures.<sup>23,62–65</sup> It is believed that rather than complex interactions between the NCs, entropy or simple sphere-packing can explain the formation of these complex phases. The aperiodicity generated through the random arrangement of equilateral triangles and squares could be a result of maximizing not only free volume entropy (packing) but also configurational entropy during the self-assembly process.<sup>23</sup> In BNSL samples, the triangles and squares correspond to the regular arrangement of (Au)<sub>6</sub> and individual Au NCs separated by Fe<sub>3</sub>O<sub>4</sub> NCs, giving rise to the so-called (3<sup>2</sup>.4.3.4) and (3<sup>3</sup>.4<sup>2</sup>) periodic Archimedean tilings with a stoichiometry of AB<sub>4</sub>.

Realizing the comparable size ratio  $\gamma$  of the 4.6 nm Au-14.0 nm Fe<sub>3</sub>O<sub>4</sub> combination in this work to the reported  $\gamma$  of  $\sim 0.43$  for quasicrystalline order in BNSLs, we further exploit the possibility of Archimedean tiling-based aperiodic ordering by adjusting the relative concentration of Au and Fe<sub>3</sub>O<sub>4</sub> NCs in the colloidal solution used for BNSL formation. When the Fe<sub>3</sub>O<sub>4</sub>-to-Au NC number ratio is lowered to  $\sim 1:5$ , we observe the formation of large-area (3<sup>2</sup>.4.3.4) tiling, together with a small fraction of bcc-AB<sub>6</sub> domains in a single sample (Figures 8 and S13, Supporting Information). The sharp spots on the fast-Fourier transform pattern from the (3<sup>2</sup>.4.3.4) tiling indicate its 4-fold rotational symmetry (Figure 8a). This suggests that in the absence of other significant interactions, entropy is the dominant driving force for BNSL formation, while fine-tuning of the concentration ratio between the constituents offers an effective means to access several candidate structures predicted by the packing argument.<sup>24,41,66</sup>

**3.5. Remarks on the Design Principles and Formation of BNSLs.** In the section, we will address several remaining issues, discuss the implications of the observation of polymorphism in AB<sub>6</sub> BNSLs, and make some general remarks on the design of BNSLs.

First, the 2D arrangement of NCs seen in the SEM image of the bcc-AB<sub>6</sub> BNSLs is interesting in its own right: surrounding each Fe<sub>3</sub>O<sub>4</sub> NCs are four pairs of smaller Au NCs. This 2D packing motif corresponding to an AB<sub>2</sub> stoichiometry is one of the densest ways to pack spheres in 2D for this particular size ratio (isostuctural to the so-called T<sub>1</sub> phase predicted by Likos et al.<sup>67</sup>). This observation might imply that during the formation of bcc-AB<sub>6</sub> BNSLs, NCs first nucleate laterally in 2D followed by growth of a few unit cells in the perpendicular direction. This may also explain the preferential orientation of the AB<sub>6</sub> BNSLs as mentioned above.

Second, we have been employing the space-filling principle to explain/understand the polymorphism in AB<sub>6</sub> BNSLs, but the space-filling factor can only tell us which crystal structures are possible, not which one will form under certain experimental

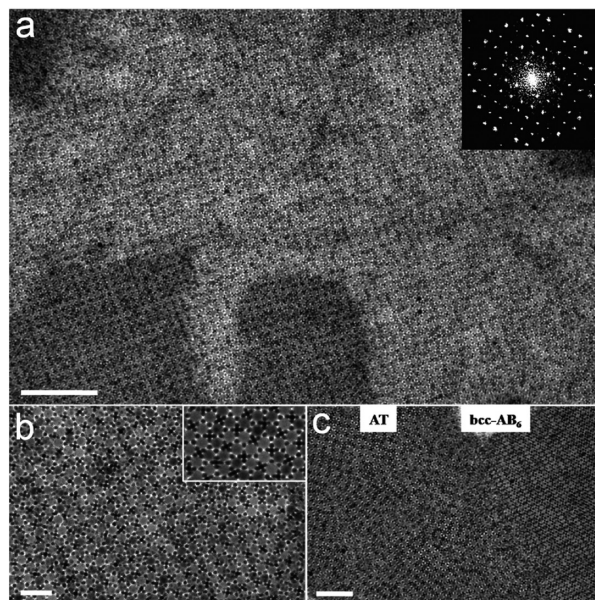


**Figure 8.** (a, b) TEM images of BNSLs self-assembled from 4.6 nm Au and 14.0 nm Fe<sub>3</sub>O<sub>4</sub> NCs exhibiting the packing motif of the periodic (3<sup>2</sup>.4.3.4) Archimedean tiling (AT). Inset of part a is the corresponding fast Fourier transform pattern of the superlattices. (c) TEM image showing the coexistence of AT and bcc-AB<sub>6</sub> BNSLs self-assembled from 4.6 nm Au and 14.0 nm Fe<sub>3</sub>O<sub>4</sub> NCs. Scale bars: (a) 200 nm, (b) 50 nm, and (c) 100 nm.

conditions. Introduction or identification of a new phase might also suggest the reduction of the “stability zone” of the existing phases. In this study, we are not able to produce phase-pure CaB<sub>6</sub> BNSLs, no matter how we adjust the number ratio between the NCs for the two size ratios, although the tunability is achieved for the case of the new polymorph—bcc-AB<sub>6</sub>.

According to the space-filling principle, a stable BNSL structure should be the one whose packing density exceeds that of the single-component close-packed structures of large and small spheres ( $\sim 0.7405$ ), although experimental results for BNSLs do not always rigorously follow the theoretical prediction. For example, the 5.8 nm Au and 14.0 nm Fe<sub>3</sub>O<sub>4</sub> NCs can form bcc-AB<sub>6</sub> BNSLs with a calculated space-filling factor  $\rho \sim 0.70$ . In fact, rigorous free energy calculations also suggest binary phases with  $\rho$  slightly below 0.7405 can still exist, being stabilized by the entropy of mixing and extra configurational entropy.<sup>68</sup> In a real binary NC system, the matter can be further complicated by the interparticle interactions.<sup>21,69–71</sup> However, we still find that theoretical phase stability calculations based upon hard sphere approximation (i.e., space-filling principle) can serve as a qualitative yet useful experimental guide to the BNSL structures expected for a given size ratio and range of the size ratios needed in order to form a particular BNSL phase. Therefore, we provide a library of space-filling curves covering the full range of radius ratios for the majority of BNSL structures that have been reported and predicted (Figure S14, Supporting Information). Several questions still remain: how can one tune the relative phase stability between the NaCl and NiAs structures which have identical space-filling curves and stoichiometry (or the same question regarding the three Lavés phases)? Is there a limit to the complexity of periodic and aperiodic BNSL phases that can be designed?<sup>72</sup> Thanks to the recent development of new deposition methodology for BNSLs, we can now access a variety of

BNSL phases over extended area ( $\text{cm}^2$  scale).<sup>24</sup> We anticipate that in the near future many known BNSL phases can become available over that length scale. On the other hand, further development of surface/ligand chemistry of colloidal NC building blocks may help the introduction of higher order or “non-hard-sphere” interparticle interactions into the colloidal NC system in a well-controlled manner, which could enrich the possible BNSL structures to be discovered.<sup>21,73</sup>

## 4. CONCLUSIONS

We have identified a new  $\text{AB}_6$  polymorph—bcc- $\text{AB}_6$ —in BNSLs composed of nearly electrostatically neutral Au and  $\text{Fe}_3\text{O}_4$  NCs through systematic electron microscopy studies. The two  $\text{AB}_6$  polymorphs— $\text{CaB}_6$  and bcc- $\text{AB}_6$ —differ in their 3D arrangement of both small and large spheres, in their lattice symmetry, and in their space-filling factor. Upon the basis of the space-filling principle, we further demonstrate the possibility of tailoring the relative phase stability between the  $\text{AB}_6$  polymorphs by adjusting the size ratio between the two NCs, highlighting the entropic contribution as the main driving force during the self-organization of NCs into BNSLs. In addition, studies of the arrangement of NCs on the BNSLs surface together with the interesting observation of twinning and preferential orientation in bcc- $\text{AB}_6$  BNSLs is indicative of a possible growth mechanism: a close-packed monolayer composed of two types of NCs forms initially followed by growth into 3D BNSLs. BNSLs exhibit unique electronic,<sup>10</sup> plasmonic,<sup>21</sup> or magnetic<sup>24</sup> couplings between the NCs, and the ability to engineer specific polymorphs provides a more powerful route to programmable physical properties.

## ■ ASSOCIATED CONTENT

**S Supporting Information.** TEM images of  $\text{Fe}_3\text{O}_4$  and Au NCs, XRD pattern of 4.6 nm Au NCs, electrophoretic mobility measurements of  $\text{Fe}_3\text{O}_4$  and Au NCs dispersed in TCE, additional TEM and SEM images showing the long-range ordering and twinning in bcc- $\text{AB}_6$  BNSLs and their coexistence with  $\text{CaB}_6$  structure and (3<sup>2</sup>.4.3.4) Archimedean tiling, tilt series of bcc- $\text{AB}_6$  BNSLs starting from [100]-oriented domains, and a library of space-filling curves and the mathematical expressions for each branch of the curves. This material is available free of charge via the Internet at <http://pubs.acs.org>.

## ■ AUTHOR INFORMATION

**Corresponding Author**  
cbmurray@sas.upenn.edu

**Author Contributions**

<sup>†</sup>These authors contributed equally.

## ■ ACKNOWLEDGMENT

We acknowledge financial support from the Department of Energy Basic Energy Science division through award DE-SC000-2158 for synthesis of plasmonic NCs and assembly and characterization of BNSLs (X.Y.) and the Army Research Office (ARO) through MURI award W911NF-08-1-0364 for support of magnetic NC synthesis and assembly and characterization of BNSLs (J.C. and C.B.M.). C.B.M. also thanks the Richard Perry University Professorship for partial support of his supervisor

role. We thank Douglas M. Yates and Lolita Rotkina at the Penn Regional Nanotechnology Facility for support in electron microscopy and Benjamin T. Diroll for manuscript proofreading and discussions.

## ■ REFERENCES

- Murray, C. B.; Kagan, C. R.; Bawendi, M. G. *Science* **1995**, *270*, 1335–1338.
- Moulton, B.; Zaworotko, M. J. *Chem. Rev.* **2001**, *101*, 1629–1658.
- Eddaoudi, M.; Moler, D. B.; Li, H. L.; Chen, B. L.; Reineke, T. M.; O’Keeffe, M.; Yaghi, O. M. *Acc. Chem. Res.* **2001**, *34*, 319–330.
- Alivisatos, A. P. *Science* **1996**, *271*, 933–937.
- Xia, Y. N.; Yang, P. D.; Sun, Y. G.; Wu, Y. Y.; Mayers, B.; Gates, B.; Yin, Y. D.; Kim, F.; Yan, Y. Q. *Adv. Mater.* **2003**, *15*, 353–389.
- Murray, C. B.; Kagan, C. R.; Bawendi, M. G. *Annu. Rev. Mater. Sci.* **2000**, *30*, 545–610.
- Pileni, M. P. *Acc. Chem. Res.* **2008**, *41*, 1799–1809.
- Nie, Z. H.; Petukhova, A.; Kumacheva, E. *Nat. Nanotechnol.* **2010**, *5*, 15–25.
- Talapin, D. V.; Murray, C. B. *Science* **2005**, *310*, 86–89.
- Urban, J. J.; Talapin, D. V.; Shevchenko, E. V.; Kagan, C. R.; Murray, C. B. *Nat. Mater.* **2007**, *6*, 115–121.
- Colvin, V. L.; Schlamp, M. C.; Alivisatos, A. P. *Nature* **1994**, *370*, 354–357.
- Coe, S.; Woo, W. K.; Bawendi, M.; Bulovic, V. *Nature* **2002**, *420*, 800–803.
- Konstantatos, G.; Howard, I.; Fischer, A.; Hoogland, S.; Clifford, J.; Klem, E.; Levina, L.; Sargent, E. H. *Nature* **2006**, *442*, 180–183.
- Huynh, W. U.; Dittmer, J. J.; Alivisatos, A. P. *Science* **2002**, *295*, 2425–2427.
- Maier, S. A.; Kik, P. G.; Atwater, H. A.; Meltzer, S.; Harel, E.; Koel, B. E.; Requicha, A. A. G. *Nat. Mater.* **2003**, *2*, 229–232.
- Anker, J. N.; Hall, W. P.; Lyandres, O.; Shah, N. C.; Zhao, J.; Van Duyne, R. P. *Nat. Mater.* **2008**, *7*, 442–453.
- Tao, A.; Sinsermsuksakul, P.; Yang, P. *Nat. Nanotechnol.* **2007**, *2*, 435–440.
- Sun, S. H.; Murray, C. B.; Weller, D.; Folks, L.; Moser, A. *Science* **2000**, *287*, 1989–1992.
- Kiely, C. J.; Fink, J.; Brust, M.; Bethell, D.; Schiffrin, D. J. *Nature* **1998**, *396*, 444–446.
- Redl, F. X.; Cho, K. S.; Murray, C. B.; O’Brien, S. *Nature* **2003**, *423*, 968–971.
- Kalsin, A. M.; Fialkowski, M.; Paszewski, M.; Smoukov, S. K.; Bishop, K. J. M.; Grzybowski, B. A. *Science* **2006**, *312*, 420–424.
- Shevchenko, E. V.; Talapin, D. V.; Kotov, N. A.; O’Brien, S.; Murray, C. B. *Nature* **2006**, *439*, 55–59.
- Talapin, D. V.; Shevchenko, E. V.; Bodnarchuk, M. I.; Ye, X. C.; Chen, J.; Murray, C. B. *Nature* **2009**, *461*, 964–967.
- Dong, A. G.; Chen, J.; Vora, P. M.; Kikkawa, J. M.; Murray, C. B. *Nature* **2010**, *466*, 474–477.
- Wang, Z. L. *Adv. Mater.* **1998**, *10*, 13–30.
- Kroto, H. W.; Heath, J. R.; Obrien, S. C.; Curl, R. F.; Smalley, R. E. *Nature* **1985**, *318*, 162–163.
- Iijima, S. *Nature* **1991**, *354*, 56–58.
- Geim, A. K.; Novoselov, K. S. *Nat. Mater.* **2007**, *6*, 183–191.
- Stephens, P. W.; Mihaly, L.; Lee, P. L.; Whetten, R. L.; Huang, S. M.; Kaner, R.; Deiderich, F.; Holczer, K. *Nature* **1991**, *351*, 632–634.
- Zhou, O.; Fischer, J. E.; Coustel, N.; Kycia, S.; Zhu, Q.; McGhie, A. R.; Romanow, W. J.; McCauley, J. P.; Smith, A. B.; Cox, D. E. *Nature* **1991**, *351*, 462–464.
- Park, J.; An, K. J.; Hwang, Y. S.; Park, J. G.; Noh, H. J.; Kim, J. Y.; Park, J. H.; Hwang, N. M.; Hyeon, T. *Nat. Mater.* **2004**, *3*, 891–895.
- Yin, Y. D.; Erdonmez, C.; Aloni, S.; Alivisatos, A. P. *J. Am. Chem. Soc.* **2006**, *128*, 12671–12673.
- Stoeva, S.; Klabunde, K. J.; Sorensen, C. M.; Dragieva, I. *J. Am. Chem. Soc.* **2002**, *124*, 2305–2311.

- (34) Pusey, P. N. *Faraday Discuss.* **2003**, *123*, 177.
- (35) Hynninen, A. P.; Christova, C. G.; van Roij, R.; van Blaaderen, A.; Dijkstra, M. *Phys. Rev. Lett.* **2006**, *96*, 138308.
- (36) Saunders, A. E.; Korgel, B. A. *ChemPhysChem* **2005**, *6*, 61–65.
- (37) Shevchenko, E. V.; Talapin, D. V.; O'Brien, S.; Murray, C. B. *J. Am. Chem. Soc.* **2005**, *127*, 8741–8747.
- (38) Shevchenko, E. V.; Talapin, D. V.; Murray, C. B.; O'Brien, S. *J. Am. Chem. Soc.* **2006**, *128*, 3620–3637.
- (39) Chen, Z. Y.; Moore, J.; Radtke, G.; Sirringhaus, H.; O'Brien, S. *J. Am. Chem. Soc.* **2007**, *129*, 15702–15709.
- (40) Smith, D. K.; Goodfellow, B.; Smilgies, D.-M.; Korgel, B. A. *J. Am. Chem. Soc.* **2009**, *131*, 3281–3290.
- (41) Chen, J.; Ye, X. C.; Murray, C. B. *ACS Nano* **2010**, *4*, 2374–2381.
- (42) Bodnarchuk, M. I.; Kovalenko, M. V.; Heiss, W.; Talapin, D. V. *J. Am. Chem. Soc.* **2010**, *132*, 11967–11977.
- (43) Overgaag, K.; Evers, W.; de Nijs, B.; Koole, R.; Meeldijk, J.; Vanmaekelbergh, D. *J. Am. Chem. Soc.* **2008**, *130*, 7833–7834.
- (44) Evers, W. H.; Nijs, B. D.; Filion, L.; Castillo, S.; Dijkstra, M.; Vanmaekelbergh, D. *Nano Lett.* **2010**, *10*, 4235–4241.
- (45) Friedrich, H.; Gommes, C. J.; Overgaag, K.; Meeldijk, J. D.; Evers, W. H.; de Nijs, B.; Boneschanscher, M. P.; de Jongh, P. E.; Verkleij, A. J.; de Jong, K. P.; van Blaaderen, A.; Vanmaekelbergh, D. *Nano Lett.* **2009**, *9*, 2719–2724.
- (46) Chen, Z.; O'Brien, S. *ACS Nano* **2008**, *2*, 1219–1229.
- (47) Sun, Z. Y.; Luo, Z. P.; Fang, J. Y. *ACS Nano* **2010**, *4*, 1821–1828.
- (48) Eldridge, M. D.; Madden, P. A.; Frenkel, D. *Nature* **1993**, *365*, 35–37.
- (49) Trizac, E.; Eldridge, M. D.; Madden, P. A. *Mol. Phys.* **1997**, *90*, 675–678.
- (50) Bolhuis, P. G.; Frenkel, D.; Mau, S. C.; Huse, D. A. *Nature* **1997**, *388*, 235–236.
- (51) Schofield, A. B.; Pusey, P. N.; Radcliffe, P. *Phys. Rev. E* **2005**, *72*, 031407.
- (52) Hynninen, A. P.; Filion, L.; Dijkstra, M. *J. Chem. Phys.* **2009**, *131*, 064902.
- (53) Frenkel, D. *Nat. Mater.* **2006**, *5*, 85–86.
- (54) Parthe, E. Z. *Kristallogr.* **1961**, *115*, 52–79.
- (55) Sanders, J. V.; Murray, M. J. *Nature* **1978**, *275*, 201–203.
- (56) Sanders, J. V. *Philos. Mag. A* **1980**, *42*, 705–720.
- (57) Murray, M. J.; Sanders, J. V. *Philos. Mag. A* **1980**, *42*, 721–740.
- (58) Pusey, P. N.; Vanmegen, W. *Nature* **1986**, *320*, 340–342.
- (59) Bartlett, P.; Ottewill, R. H.; Pusey, P. N. *Phys. Rev. Lett.* **1992**, *68*, 3801–3804.
- (60) Velikov, K. P.; Christova, C. G.; Dullens, R. P. A.; van Blaaderen, A. *Science* **2002**, *296*, 106–109.
- (61) Rupich, S. M.; Shevchenko, E. V.; Bodnarchuk, M. I.; Lee, B.; Talapin, D. V. *J. Am. Chem. Soc.* **2010**, *132*, 289–296.
- (62) Zeng, X. B.; Ungar, G.; Liu, Y. S.; Percec, V.; Dulcey, S. E.; Hobbs, J. K. *Nature* **2004**, *428*, 157–160.
- (63) Abe, E.; Yan, Y. F.; Pennycook, S. J. *Nat. Mater.* **2004**, *3*, 759–767.
- (64) Keys, A. S.; Glotzer, S. C. *Phys. Rev. Lett.* **2007**, *99*, 235503.
- (65) van Blaaderen, A. *Nature* **2009**, *461*, 892–893.
- (66) Evers, W. H.; Friedrich, H.; Filion, L.; Dijkstra, M.; Vanmaekelbergh, D. *Angew. Chem., Int. Ed.* **2009**, *48*, 9655–9657.
- (67) Likos, C. N.; Henley, C. L. *Philos. Mag. B* **1993**, *68*, 85–113.
- (68) Xu, H.; Baus, M. *J. Phys.: Condens. Matter* **1992**, *4*, L663–L668.
- (69) Bishop, K. J. M.; Wilmer, C. E.; Soh, S.; Grzybowski, B. A. *Small* **2009**, *5*, 1600–1630.
- (70) Min, Y. J.; Akbulut, M.; Kristiansen, K.; Golan, Y.; Israelachvili, J. *Nat. Mater.* **2008**, *7*, 527–538.
- (71) Lalatonne, Y.; Richardi, J.; Pilani, M. P. *Nat. Mater.* **2004**, *3*, 121–125.
- (72) Hart, G. L. W. *Nat. Mater.* **2007**, *6*, 941–945.
- (73) Leunissen, M. E.; Christova, C. G.; Hynninen, A. P.; Royall, C. P.; Campbell, A. I.; Imhof, A.; Dijkstra, M.; van Roij, R.; van Blaaderen, A. *Nature* **2005**, *437*, 235–240.

# Supporting Information

## Polymorphism in Self-Assembled AB<sub>6</sub> Binary Nanocrystal Superlattices

Xingchen Ye<sup>1, †</sup>, Jun Chen<sup>2, †</sup>, Christopher B. Murray<sup>1, 2, \*</sup>

<sup>1</sup>Department of Chemistry, University of Pennsylvania, Philadelphia, PA 19104, USA

<sup>2</sup>Department of Materials Science and Engineering, University of Pennsylvania, Philadelphia,  
PA 19104, USA

<sup>†</sup>These authors contributed equally to this work

\* To whom correspondence should be addressed. E-mail: [cbmurray@sas.upenn.edu](mailto:cbmurray@sas.upenn.edu)

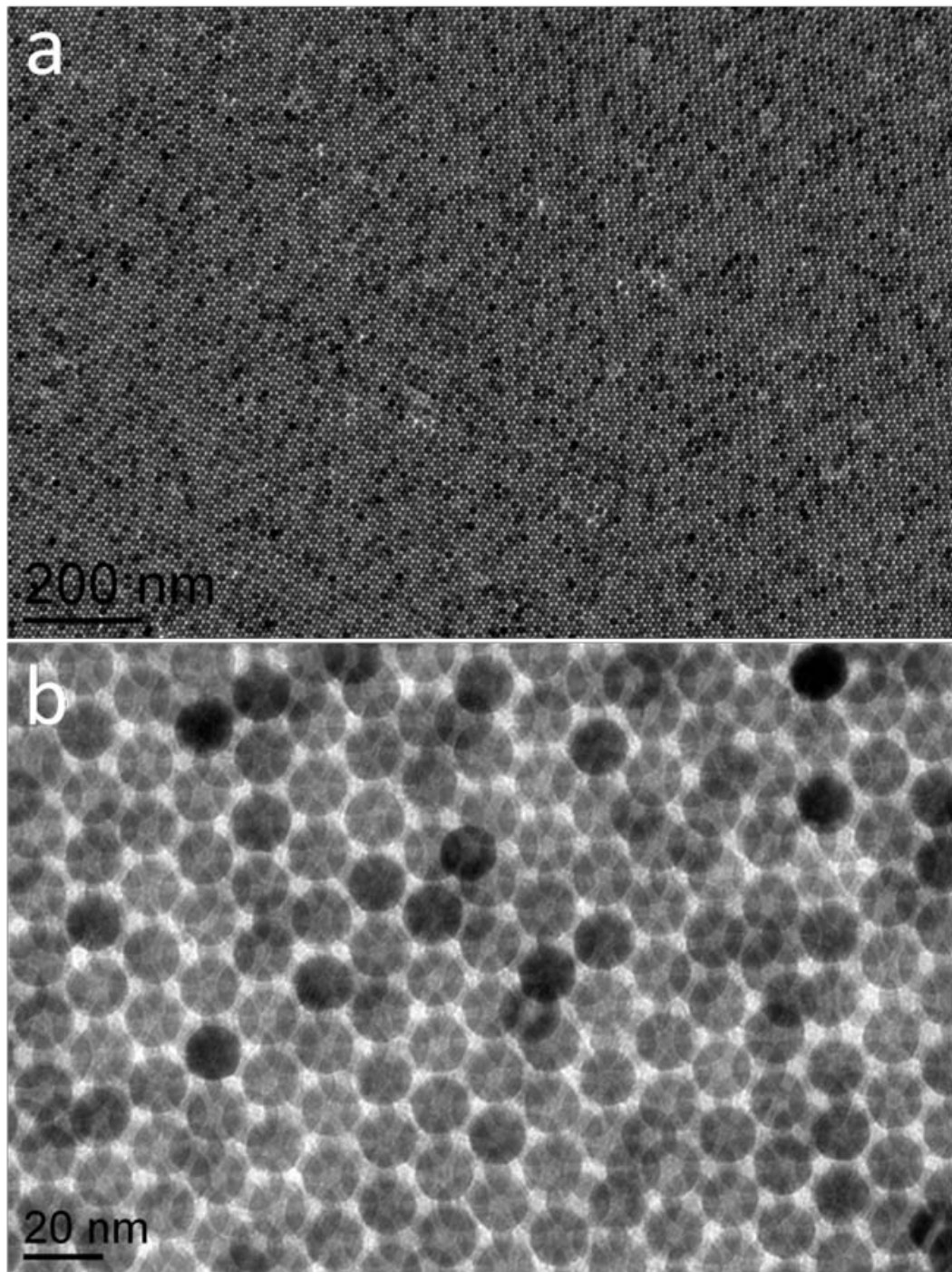


**Figure S1.** (a) Low and (b) high magnification TEM images of 14.0 nm  $\text{Fe}_3\text{O}_4$  NCs.

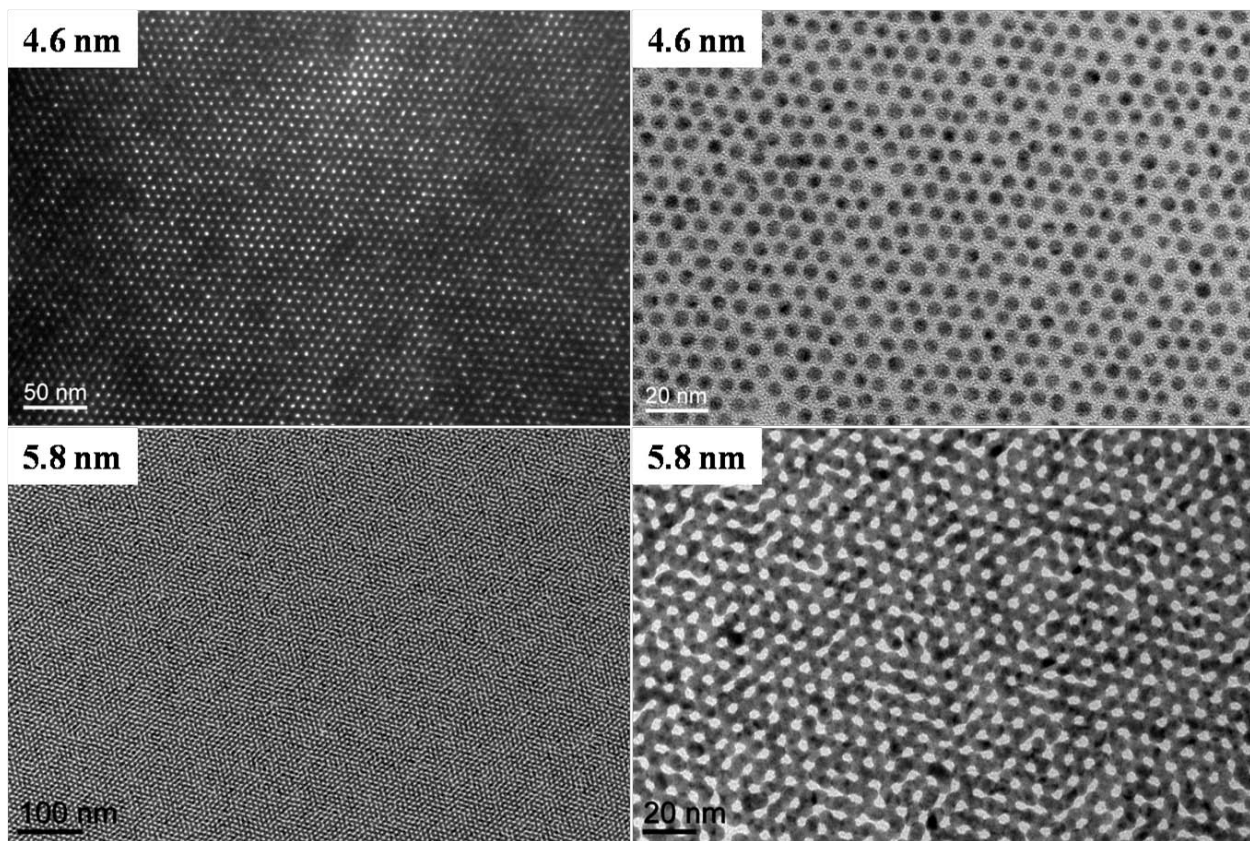


**Figure S2.** TEM images of 4.6 nm and 5.8 nm Au NCs.

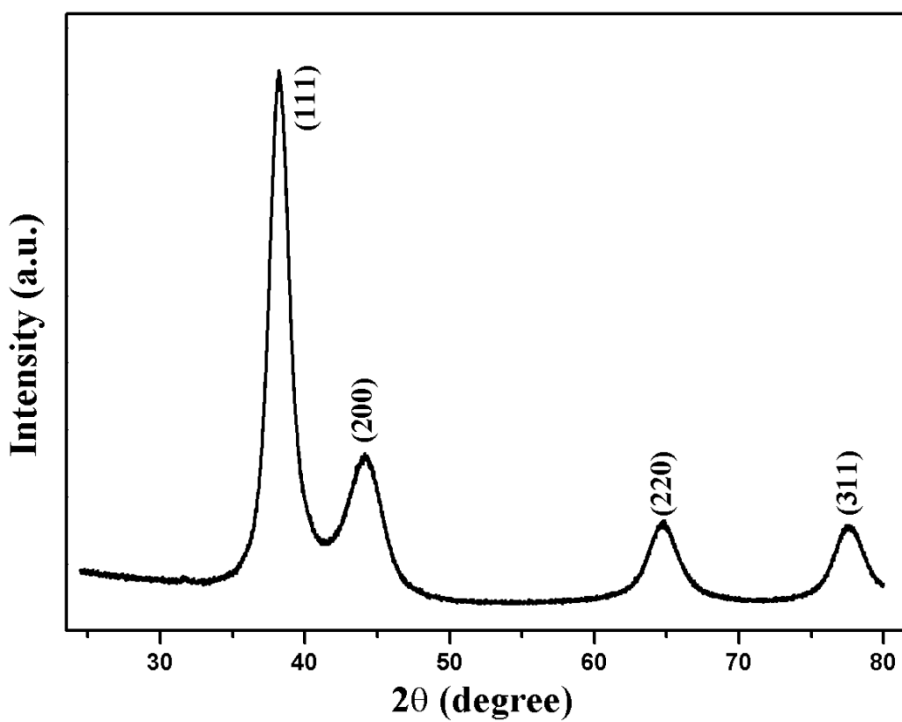


**Figure S3.** Powder XRD pattern of the 4.6 nm Au NCs.

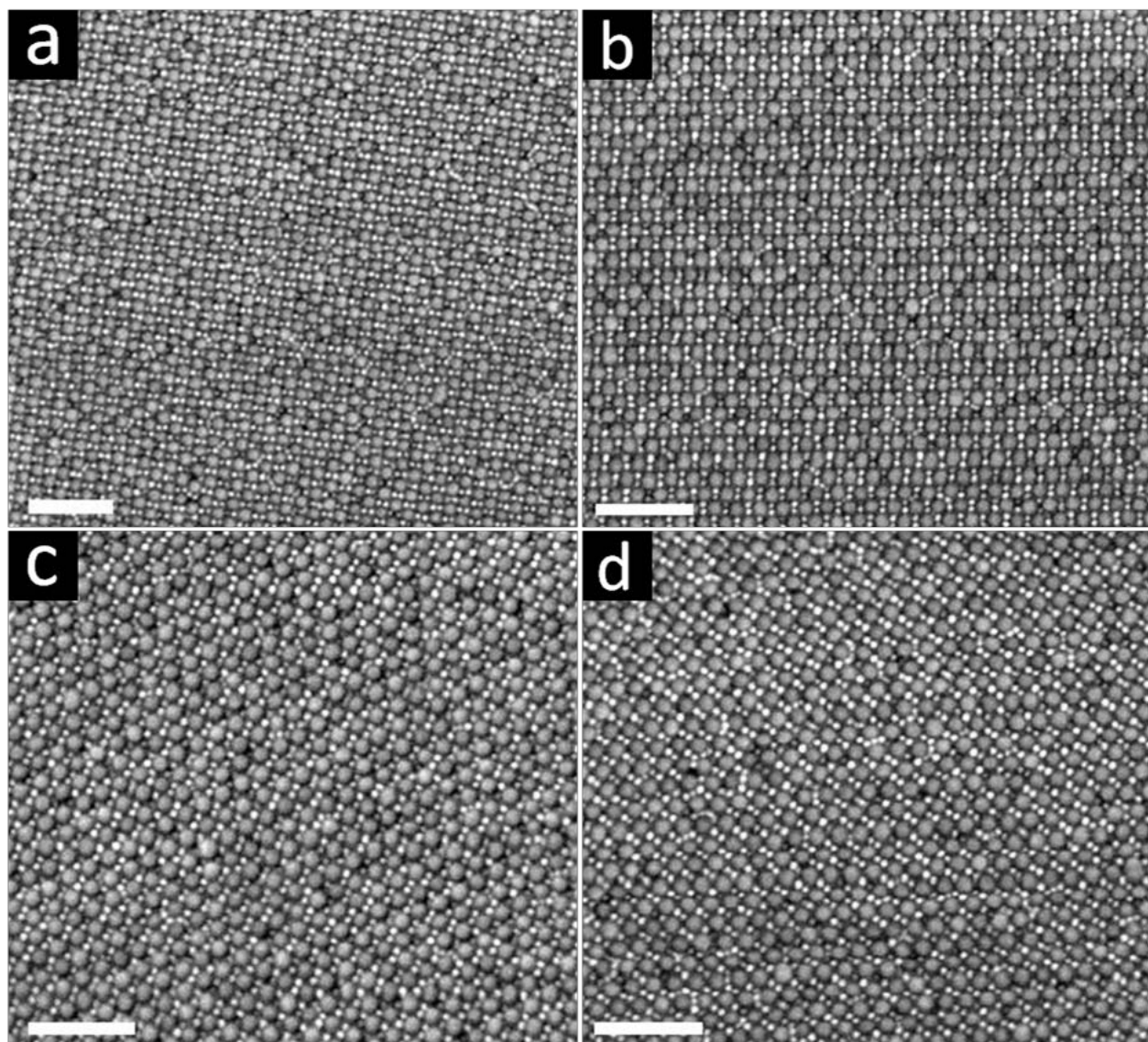


**Figure S4.** Additional SEM images taken from two different samples of bcc-AB<sub>6</sub> BNSLs self-assembled from 4.6 nm Au and 14.0 nm Fe<sub>3</sub>O<sub>4</sub> NCs. All scale bars represent 100 nm.

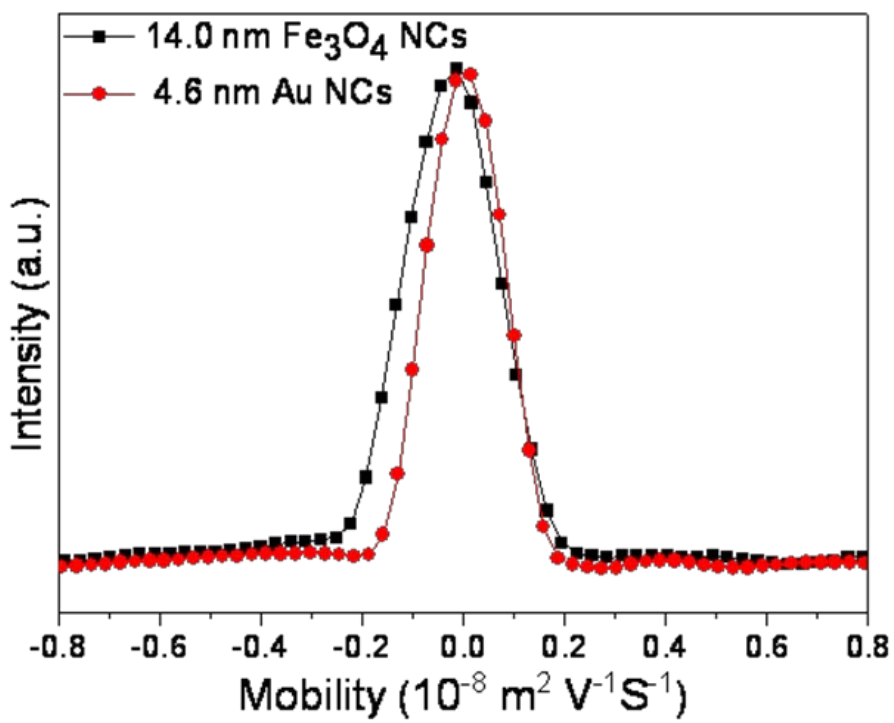


**Figure S5.** Electrophoretic mobility measurements of 4.6 nm Au and 14.0 nm  $\text{Fe}_3\text{O}_4$  NCs dispersed in TCE.

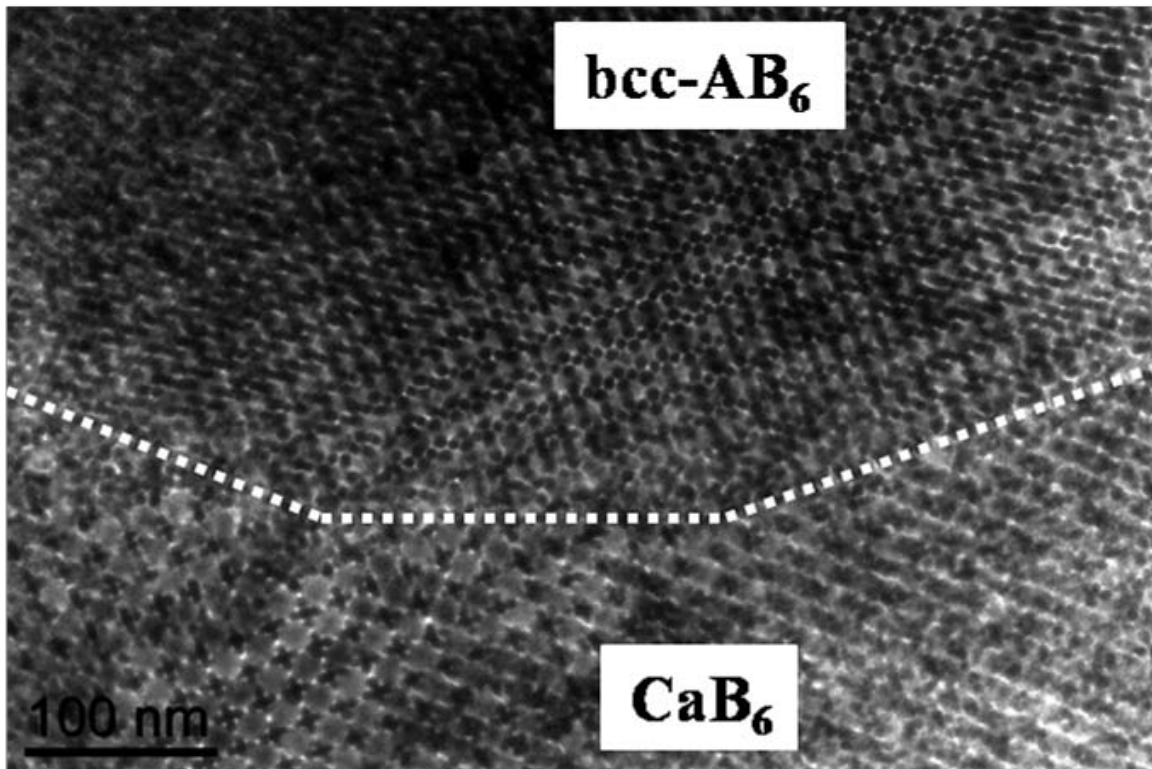


**Figure S6.** Additional TEM image of the twin boundary in bcc-AB<sub>6</sub> BNSLs self-assembled from 4.6 nm Au and 14.0 nm  $\text{Fe}_3\text{O}_4$  NCs.

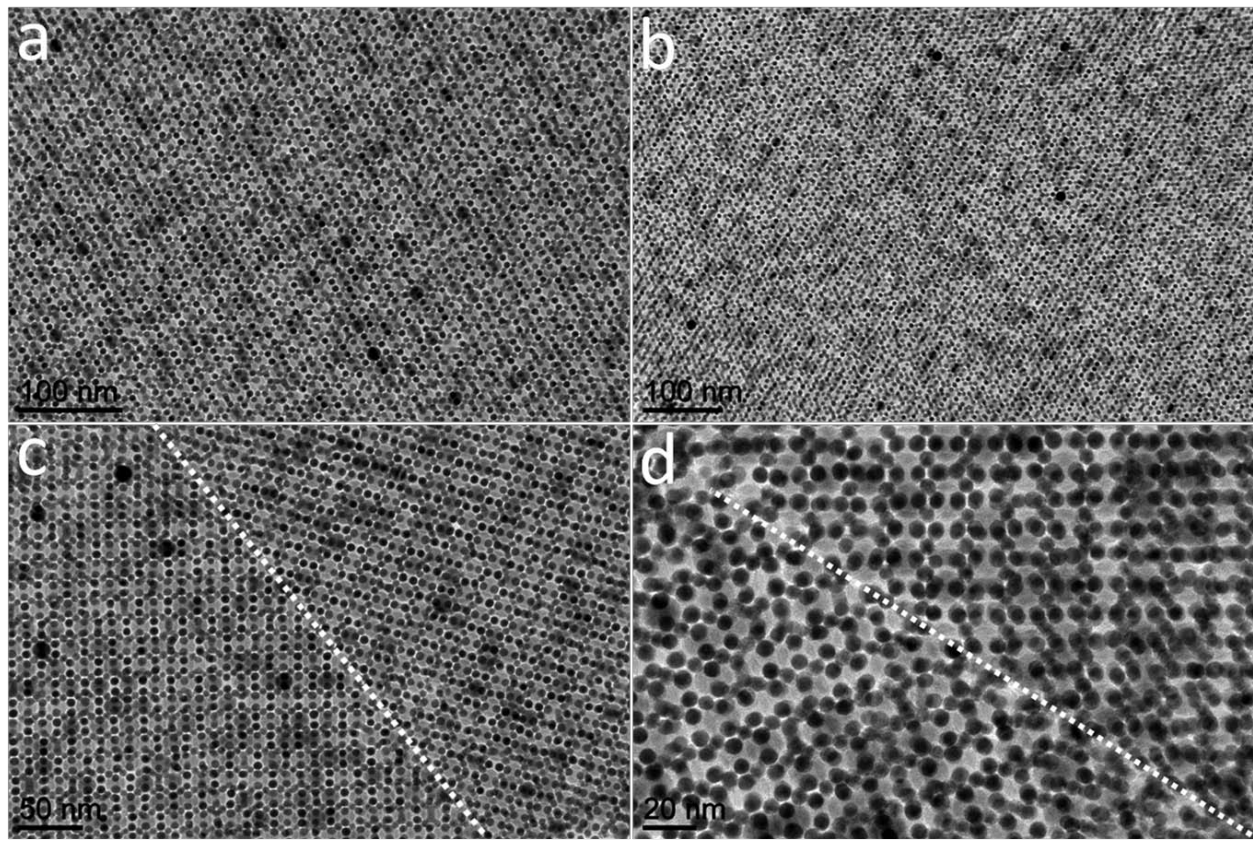


**Figure S7.** TEM images of the bcc-AB<sub>6</sub> (a, b) and the twin boundaries (c, d) in bcc-AB<sub>6</sub> BNSLs self-assembled using the interfacial assembly method (diethylene glycol was employed as the liquid subphase) recently developed by our group (ref. 24). 10  $\mu$ L hexane solution of 14.0 nm Fe<sub>3</sub>O<sub>4</sub> NCs (~3.0 mg/mL) was mixed together with 20  $\mu$ L hexane solution of 5.8 nm Au NCs (~1.0 mg/mL) in a vial and the resulting mixture was used for deposition (~1:6.5 Fe<sub>3</sub>O<sub>4</sub>-to-Au NC number ratio). This further supports that the bcc-AB<sub>6</sub> structure is a stable phase that is not subject to the deposition methodology.

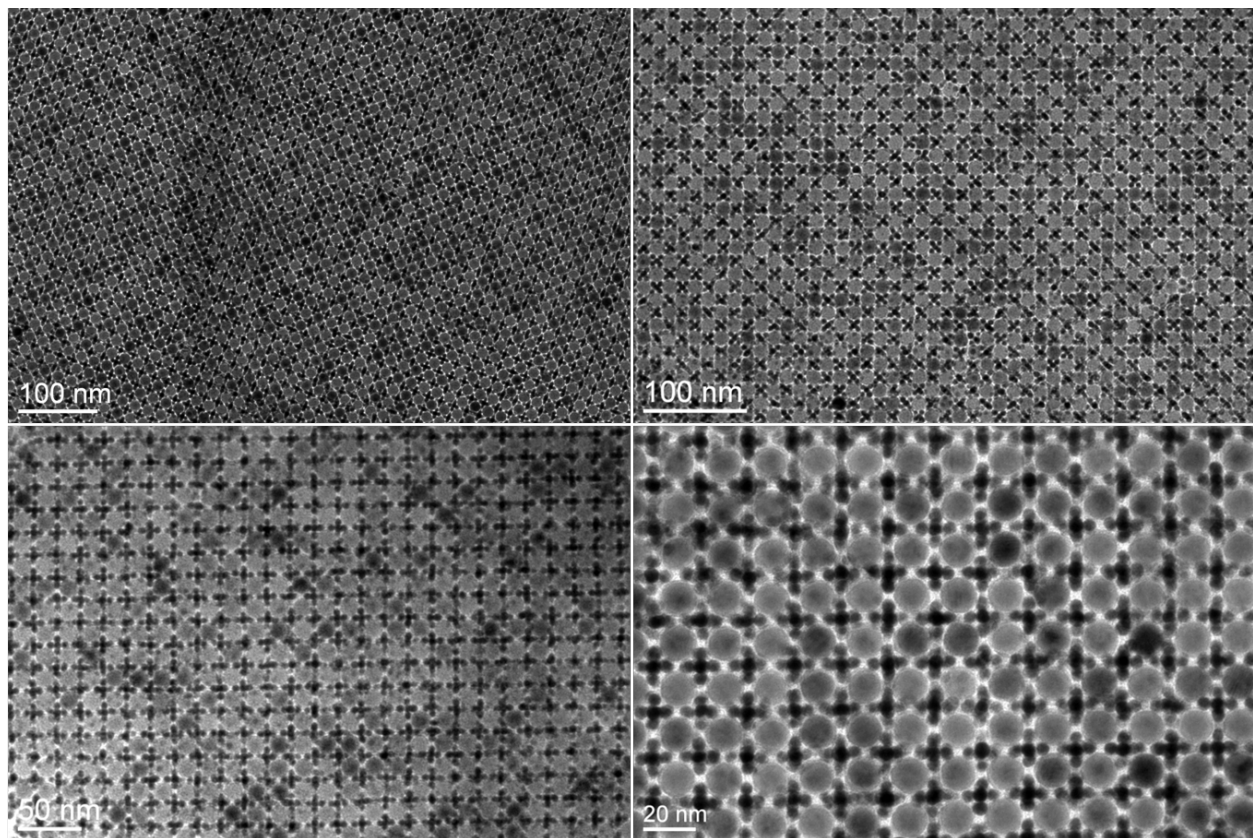


**Figure S8.** Additional TEM images taken from two different samples of  $\text{CaB}_6$  BNSLs self-assembled from 4.6 nm Au and 14.0 nm  $\text{Fe}_3\text{O}_4$  NCs.

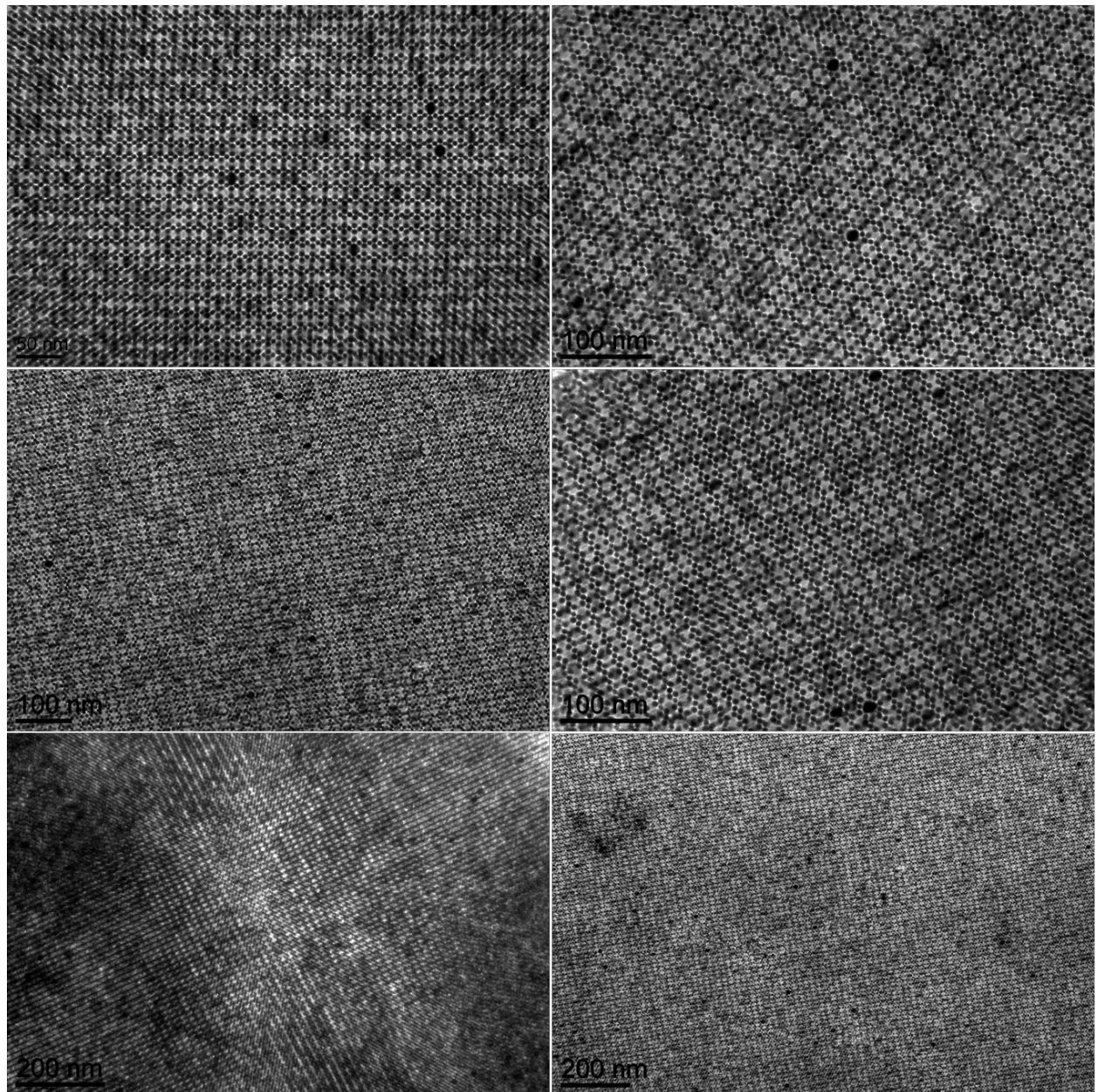


**Figure S9.** Additional TEM images taken from four different samples of bcc- $\text{AB}_6$  BNSLs self-assembled from 4.6 nm Au and 14.0 nm  $\text{Fe}_3\text{O}_4$  NCs.

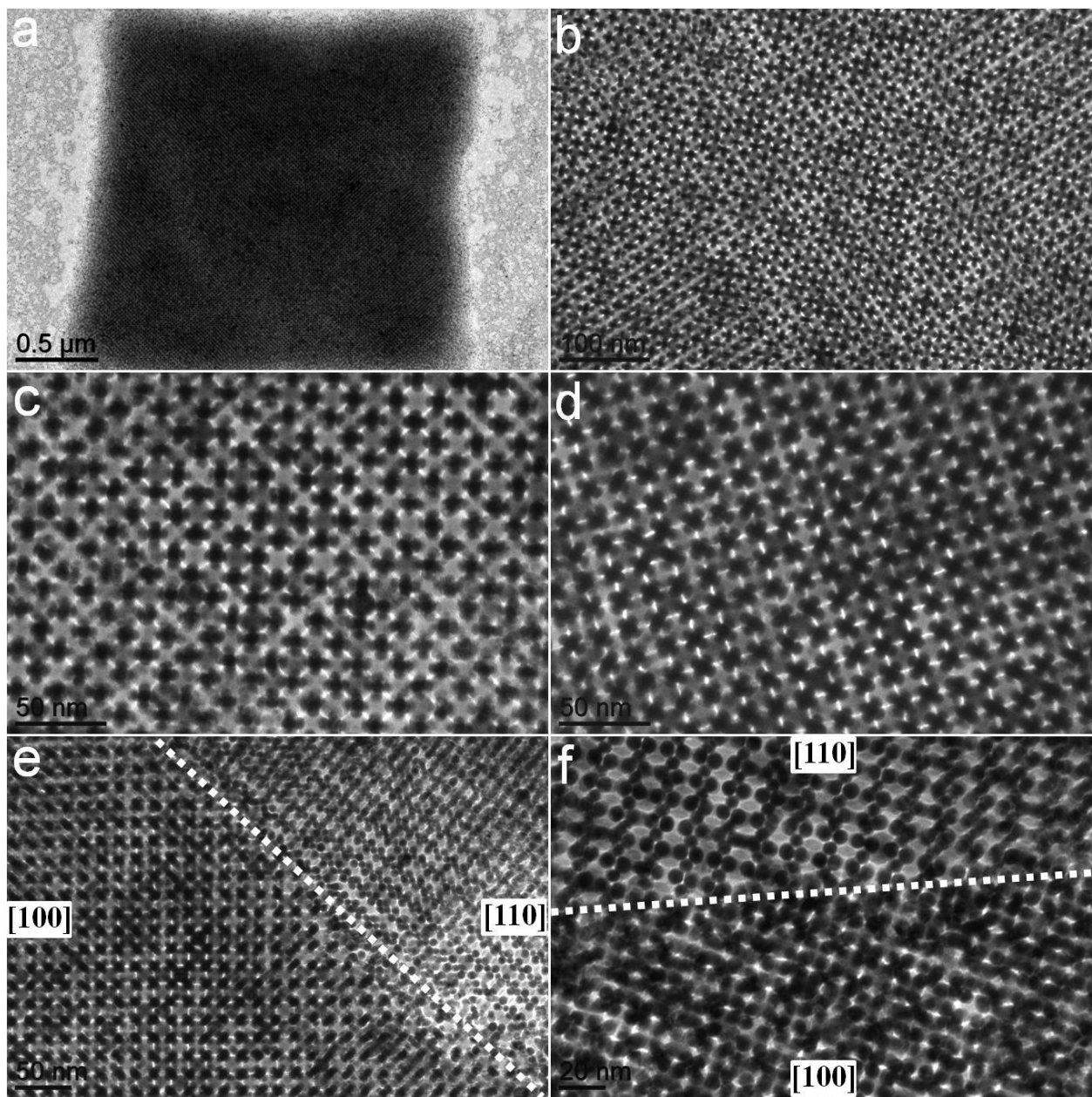


**Figure S10.** (a-d) Additional TEM images of [100]-oriented domains of bcc-AB<sub>6</sub> BNSLs self-assembled from 5.8 nm Au and 14.0 nm Fe<sub>3</sub>O<sub>4</sub> NCs. (e, f) Additional TEM images showing the coexistence of [100]-and [110]-oriented domains in bcc-AB<sub>6</sub> BNSLs self-assembled from 5.8 nm Au and 14.0 nm Fe<sub>3</sub>O<sub>4</sub> NCs.

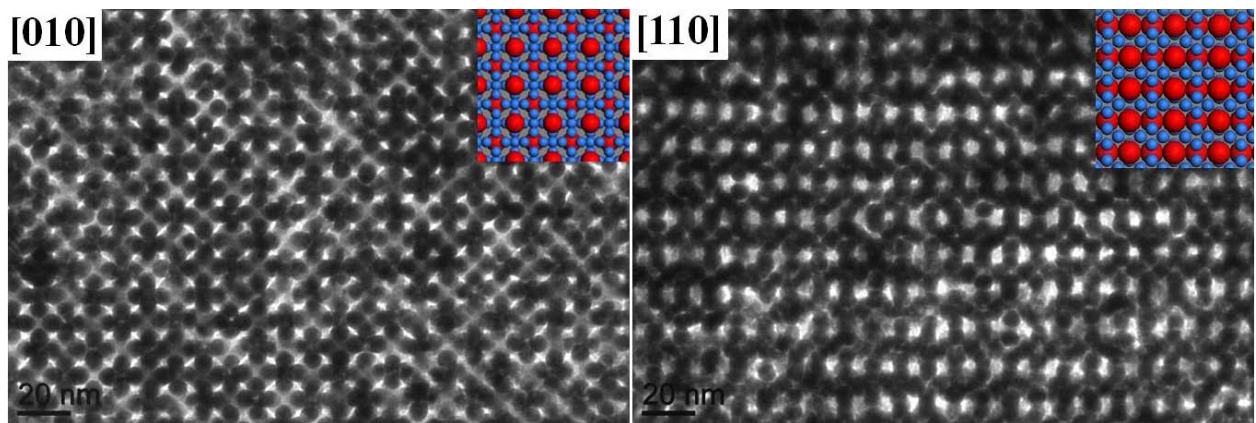


**Figure S11.** Series tilting of bcc-AB<sub>6</sub> BNSLs self-assembled from 5.8 nm Au and 14.0 nm Fe<sub>3</sub>O<sub>4</sub> NCs. The tilt series starts from [010] zone axis, tilts around [001] direction and ends up with [110] zone axis. Insets are the corresponding structural models.

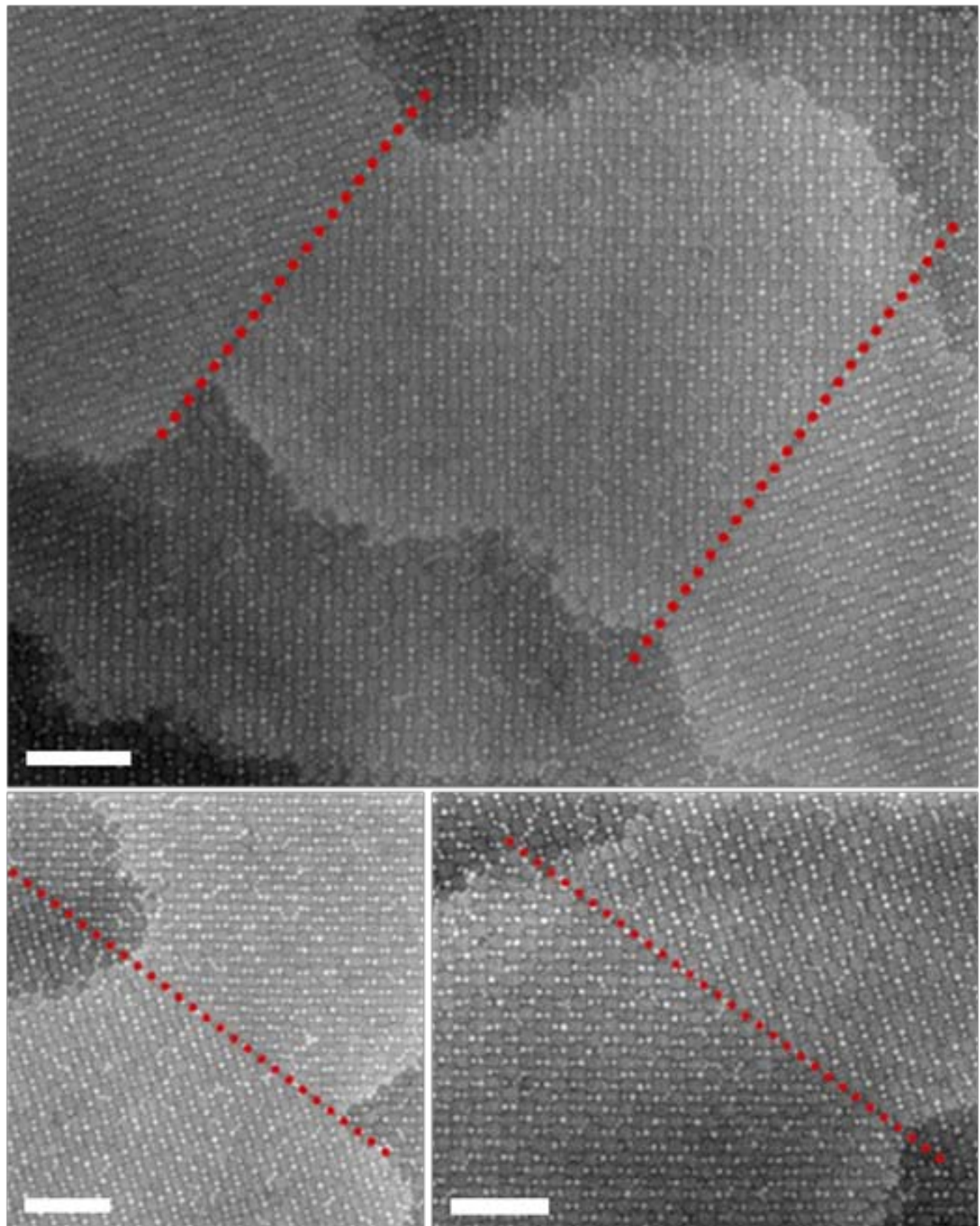


**Figure S12.** SEM images showing the twin boundary (highlighted by red dashed lines) in bcc- $\text{AB}_6$  BNSLs self-assembled from 4.6 nm Au and 14.0 nm  $\text{Fe}_3\text{O}_4$  NCs. All scale bars represent 100 nm.

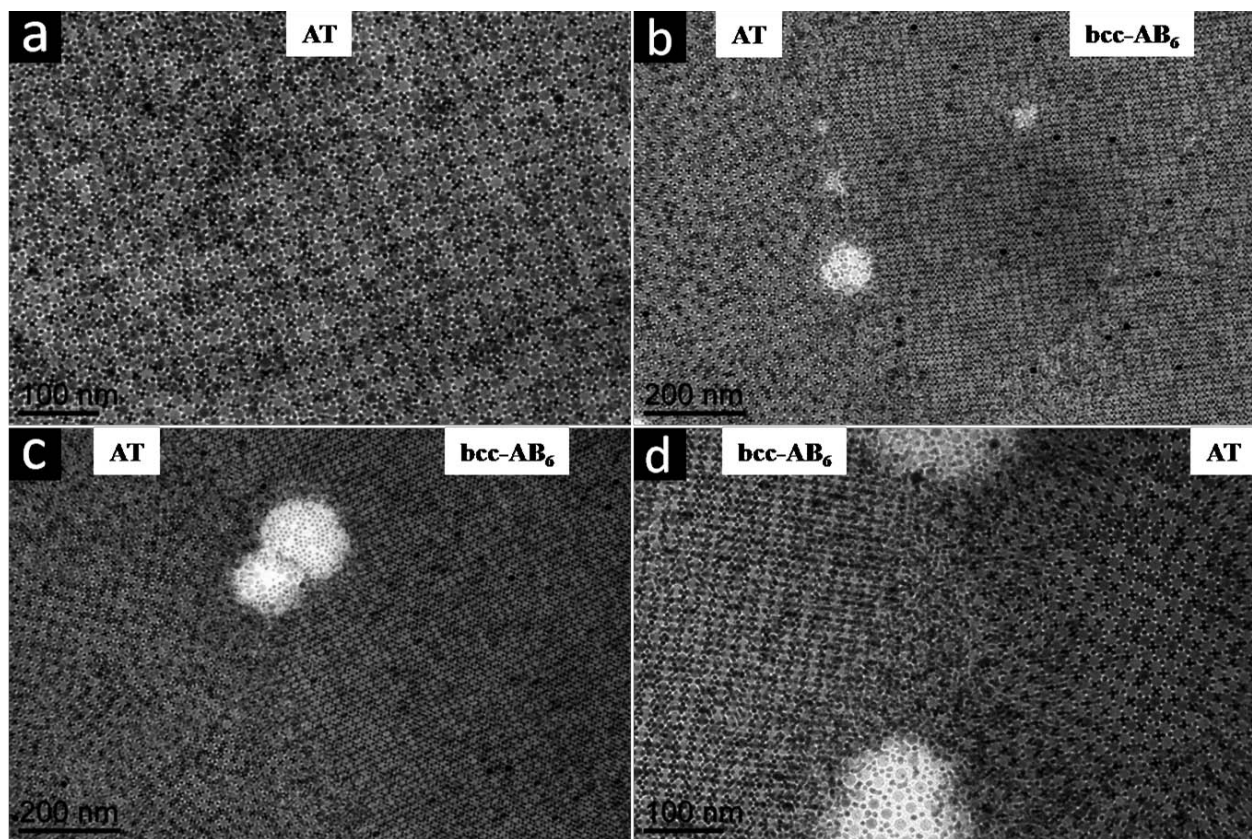


**Figure S13.** Additional TEM images showing the periodic (3<sup>2</sup>.4.3.4) Archimedean tiling (a) and the coexistence of (3<sup>2</sup>.4.3.4) Archimedean tiling and bcc-AB<sub>6</sub> in BNSLs self-assembled from 4.6 nm Au and 14.0 nm Fe<sub>3</sub>O<sub>4</sub> NCs.

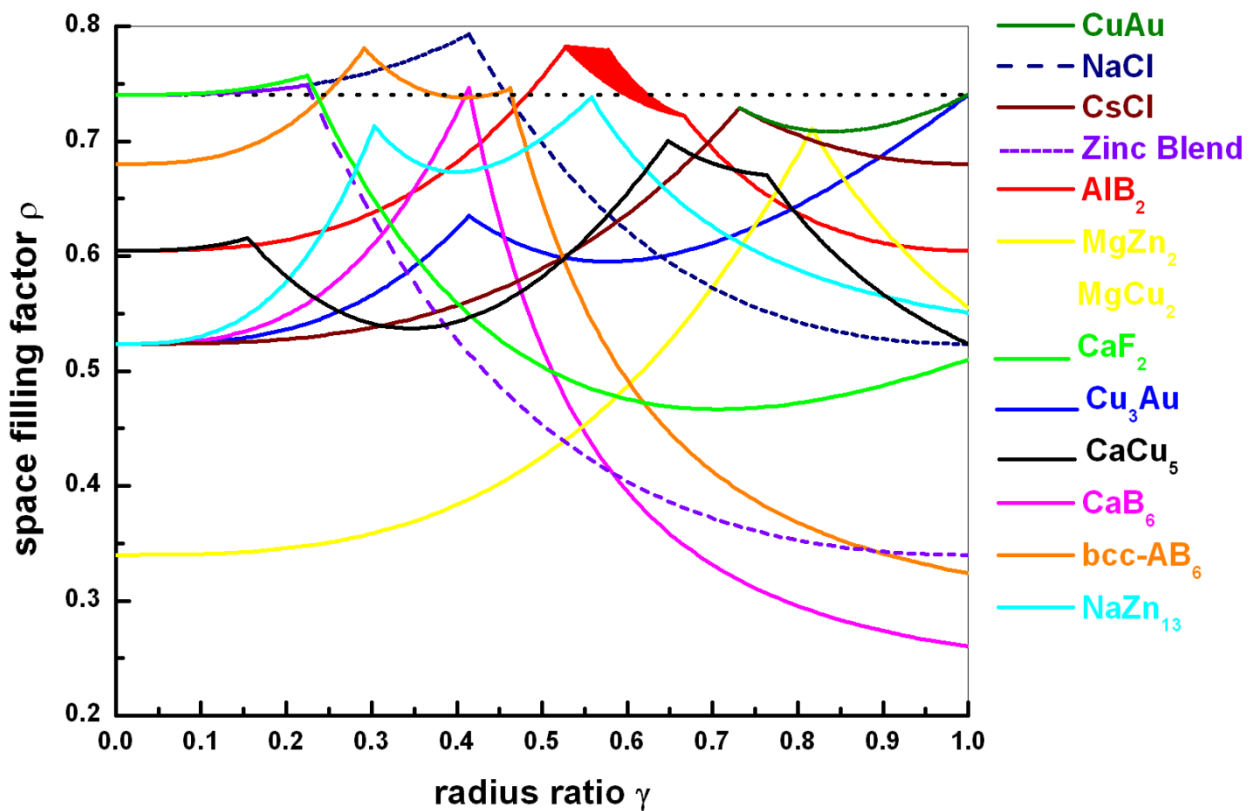


**Figure S14.** Space-filling curves of various binary structures that have been observed in BNSLs. The black dashed line represents the packing density  $\rho=0.7405$  of the single-component close-packed structures. The filled-in section in the  $\text{AlB}_2$  curve corresponds to different configurations of densely packed spheres.

**Table S1.** Mathematical expressions of packing density of CuAu structure<sup>1</sup>

packing density expressions of CuAu structure	radius ratio range	conditions
$\rho(\gamma) = \frac{\pi(1+\gamma^3)}{6}$	$0 < \gamma < 0.732$	A-A contact only*
$\rho(\gamma) = \frac{\pi(1+\gamma^3)}{6(\gamma^2+2\gamma-1)^{1/2}}$	$0.732 \leq \gamma < 1$	A-A contact in the basal plane and A-B contact

\*note: “A” represents the larger spheres while “B” represents the smaller ones.  $\gamma = r_B/r_A$ . These notations apply to the following tables as well.

**Table S2.** Mathematical expressions of packing density of NaCl structure<sup>2</sup>

packing density expressions of NaCl structure	radius ratio range	conditions
$\rho(\gamma) = \frac{\sqrt{2}\pi(1+\gamma^3)}{6}$	$0 < \gamma < 0.414$	A-A contact only
$\rho(\gamma) = \frac{2\pi(1+\gamma^3)}{3(1+\gamma)^3}$	$0.414 \leq \gamma < 1$	A-B contact only

**Table S3.** Mathematical expressions of packing density of CsCl structure<sup>2</sup>

packing density expressions of CsCl structure	radius ratio range	conditions
$\rho(\gamma) = \frac{\pi(1+\gamma^3)}{6}$	$0 < \gamma < 0.732$	A-A contact only
$\rho(\gamma) = \frac{\sqrt{3}\pi(1+\gamma^3)}{2(1+\gamma)^3}$	$0.732 \leq \gamma < 1$	A-B contact only

**Table S4.** Mathematical expressions of packing density of Zinc Blend structure<sup>2</sup>

packing density expressions of Zinc Blend structure	radius ratio range	conditions
$\rho(\gamma) = \frac{\sqrt{2}\pi(1+\gamma^3)}{6}$	$0 < \gamma < 0.2247$	A-A contact only
$\rho(\gamma) = \frac{\sqrt{3}\pi(1+\gamma^3)}{4(1+\gamma)^3}$	$0.2247 \leq \gamma < 1$	A-B contact only

**Table S5.** Mathematical expressions of packing density of AlB<sub>2</sub> structure<sup>3</sup>

packing density expressions of AlB <sub>2</sub> structure	radius ratio range	conditions
$\rho(\gamma) = \frac{\pi(1+2\gamma^3)}{3\sqrt{3}}$	$0 < \gamma < 0.527$	A-A contact only
$\rho(\gamma) = \frac{\pi(1+2\gamma^3)}{3\sqrt{3}[(1+\gamma)^2 - \frac{4}{3}]^{1/2}}$	$0.527 \leq \gamma < 0.577$	A-A contact in the basal plane with A-B contact
$\rho(\gamma) = \frac{4\pi(1+2\gamma^3)}{9\sqrt{3}(\gamma^2+2\gamma)}$	$0.527 \leq \gamma < 0.667$	A-A contact across the basal plane with A-B contact
$\rho(\gamma) = \frac{\pi(1+2\gamma^3)}{9\sqrt{3}\gamma^2(1+2\gamma-3\gamma^2)^{1/2}}$	$0.577 \leq \gamma < 0.667$	A-B contact with B-B contact in the basal plane
$\rho(\gamma) = \frac{\pi(1+2\gamma^3)}{9\sqrt{3}\gamma^2}$	$0.667 \leq \gamma < 1$	A-A contact across the basal plane with B-B contact in the basal plane

**Table S6.** Mathematical expressions of packing density of MgZn<sub>2</sub> structure<sup>2</sup>

packing density expressions of MgZn <sub>2</sub> structure	radius ratio range	conditions
$\rho(\gamma) = \frac{\sqrt{3}\pi}{16}(1 + 2\gamma^3)$	$0 < \gamma < 0.816$	A-A contact only
$\rho(\gamma) = \frac{\sqrt{2}\pi(1 + 2\gamma^3)}{24\gamma^3}$	$0.816 \leq \gamma < 1$	A-B contact only

**Table S7.** Mathematical expressions of packing density of CaF<sub>2</sub> structure<sup>2</sup>

packing density expressions of CaF <sub>2</sub> structure	radius ratio range	conditions
$\rho(\gamma) = \frac{\sqrt{2}\pi}{6}(1 + 2\gamma^3)$	$0 < \gamma < 0.2247$	A-A contact only
$\rho(\gamma) = \frac{\sqrt{3}\pi(1 + 2\gamma^3)}{4(1 + \gamma)^3}$	$0.2247 \leq \gamma < 1$	A-B contact only

**Table S8.** Mathematical expressions of packing density of Cu<sub>3</sub>Au structure<sup>1</sup>

packing density expressions of Cu <sub>3</sub> Au structure	radius ratio range	conditions
$\rho(\gamma) = \frac{\pi}{2} \left( \gamma^3 + \frac{1}{3} \right)$	$0 < \gamma < 0.414$	A-A contact only
$\rho(\gamma) = \frac{\sqrt{2}\pi \left( \gamma^3 + \frac{1}{3} \right)}{(1+\gamma)^3}$	$0.414 \leq \gamma < 1$	A-B contact only

**Table S9.** Mathematical expressions of packing density of CaCu<sub>5</sub> structure<sup>4</sup>

packing density expressions of CaCu <sub>5</sub> structure	radius ratio range	conditions
$\rho(\gamma) = \frac{\pi(1+5\gamma^3)}{3\sqrt{3}}$	$0 < \gamma < 0.1547$	A-A contact only
$\rho(\gamma) = \frac{4\pi(1+5\gamma^3)}{9\sqrt{3}(1+\gamma)^2}$	$0.1547 \leq \gamma < 0.6478$	A-B contact in the basal planes
$\rho(\gamma) = \frac{8\pi(1+5\gamma^3)}{9\sqrt{3}(1+\gamma)^2 \sqrt{15\gamma^2 - 2\gamma - 1}}$	$0.6478 \leq \gamma < 0.7637$	B-B contact in adjacent basal planes
$\rho(\gamma) = \frac{\pi(1+5\gamma^3)}{6\sqrt{3}\gamma^2 \sqrt{15\gamma^2 - 2\gamma - 1}}$	$0.7637 \leq \gamma < 1$	B-B contact in the basal planes of pure B spheres

**Table S10.** Mathematical expressions of packing density of CaB<sub>6</sub> structure<sup>5</sup>

packing density expressions of CaB <sub>6</sub> structure	radius ratio range	conditions
$\rho(\gamma) = \pi \left( \gamma^3 + \frac{1}{6} \right)$	$0 < \gamma < 0.414$	A-A contact and B-B contact in the same unit cell
$\rho(\gamma) = \frac{0.03715}{\gamma^3} + 0.2229$	$0.414 \leq \gamma < 1$	B-B contact in the same unit cell as well as in the neighboring unit cell

**Table S11.** Mathematical expressions of packing density of bcc-AB<sub>6</sub> structure

packing density expressions of bcc-AB <sub>6</sub> structure	radius ratio range	conditions
$\rho = \frac{\sqrt{3}\pi}{8}(1 + 6\gamma^3)$	$0 < \gamma < 0.291$	A-A contact only
$\rho = \frac{5\sqrt{5}\pi}{24}(1+6\gamma^3)(1+\gamma)^3$	$0.291 \leq \gamma < 0.462$	A-A contact and A-B contact
$\rho = \frac{\sqrt{2}\pi}{96}(6+\frac{1}{\gamma^3})$	$0.462 \leq \gamma < 1$	B-B contact only

**Table S12.** Mathematical expressions of packing density of NaZn<sub>13</sub> structure<sup>3</sup>

packing density expressions of NaZn <sub>13</sub> structure	radius ratio range	conditions
$\rho(\gamma) = \frac{4\pi(1 + 13\gamma^3)}{3}$	$0 < \gamma < 0.303$	A-A contact only
$\rho(\gamma) = \frac{4\pi(1 + 13\gamma^3) * 1.9021\sqrt{3}}{3\gamma^3 * 4\sqrt{(1.9021^2 - \frac{4}{3})}} + 2$ $* (1 + \gamma)^2 - \sqrt{\frac{16\gamma^2}{3 * 1.9021^2} * (\sqrt{3}\gamma)^{1/3}}$	$0.303 \leq \gamma < 0.558$	A-B contact and B-B contact within the subcell only
$\rho(\gamma) = \frac{\pi(1 + 13\gamma^3)}{6 * 2.370032^3 * \gamma^3}$	$0.558 \leq \gamma < 1$	B-B contact only

## **Supporting References:**

- (1) Bodnarchuk, M. I.; Kovalenko, M. V.; Heiss, W.; Talapin, D. V. *J. Am. Chem. Soc.* **2010**, *132*, 11967-11977.
- (2) Parthe, E. Z. *Kristallogr.* **1961**, *115*, 52–79.
- (3) Murray, M. J.; Sanders, J. V. *Philos. Mag. A* **1980**, *42*, 721-740.
- (4) Chen, Z. Y.; Moore, J.; Radtke, G.; Sirringhaus, H.; O'Brien, S. *J. Am. Chem. Soc.* **2007**, *129*, 15702-15709.
- (5) Talapin, D. V.; Shevchenko, E. V.; Bodnarchuk, M. I.; Ye, X. C.; Chen, J.; Murray, C. B. *Nature* **2009**, *461*, 964-967.